

GPTR: Gaussian Process Trajectory Representation for Continuous-Time Motion Estimation

Thien-Minh Nguyen, *Member, IEEE*, Ziyu Cao, *Student Member, IEEE*, Kailai Li, *Member, IEEE*,
Shenghai Yuan, *Member, IEEE*, Lihua Xie, *Fellow, IEEE*,

Abstract—Continuous-time trajectory representation has gained significant popularity in recent years, as it offers an elegant formulation that allows the fusion of a larger number of sensors and sensing modalities, overcoming limitations of traditional discrete-time frameworks. To bolster the adoption of the continuous-time paradigm, we propose a so-called Gaussian Process Trajectory Representation (GPTR) framework for continuous-time motion estimation (CTME) tasks. Our approach stands out by employing a third-order random jerk model, featuring closed-form expressions for both rotational and translational state derivatives. This model provides smooth, continuous trajectory representations that are crucial for precise estimation of complex motion. To support the wider robotics and computer vision communities, we have made the source code for GPTR available as a light-weight header-only library. This format was chosen for its ease of integration, allowing developers to incorporate GPTR into existing systems without needing extensive code modifications. Moreover, we also provide a set of optimization examples with LiDAR, camera, IMU, UWB factors, and closed-form analytical Jacobians under the proposed GP framework. Our experiments demonstrate the efficacy and efficiency of GP-based trajectory representation in various motion estimation tasks, and the examples can serve as the prototype to help researchers quickly develop future applications such as batch optimization, calibration, sensor fusion, trajectory planning, etc., with continuous-time trajectory representation. Our project is accessible at <https://github.com/brytsknguyen/gptr>.

I. INTRODUCTION

In recent years, continuous-time trajectory representation has gained significant popularity in robotics motion estimation tasks. In this domain, continuous-time motion estimation (CTME) rectifies several disadvantages of the conventional discrete-time (DT) approach, the biggest of which is that it restricts the coupling of observations with the few chosen discrete states, leading to some compromises (Fig. 1). On the other hand, continuous-time estimation approaches allow one to directly fuse sensor measurements at the sample acquisition time. This is very useful for high-frequency and temporally spread-out sensors such as IMU, event camera, LiDAR, etc.

Thien-Minh Nguyen, Shenghai Yuan and Lihua Xie are with the School of Electrical and Electronic Engineering, Nanyang Technological University, 50 Nanyang Avenue, Singapore 639798. Ziyu Cao is with the Department of Electrical Engineering, Linköping University, 58183 Linköping, Sweden. Kailai Li is with the Bernoulli Institute for Mathematics, Computer Science and Artificial Intelligence, University of Groningen, 9747 AG Groningen, the Netherlands. (e-mail: {thienminh.nguyen, shyuan, elhxie}@ntu.edu.sg, ziyu.cao@liu.se, kailai.li@rug.nl). Corresponding author: Thien-Minh Nguyen

This research is supported by the National Research Foundation, Singapore under its Medium Sized Center for Advanced Robotics Technology Innovation (CARTIN).

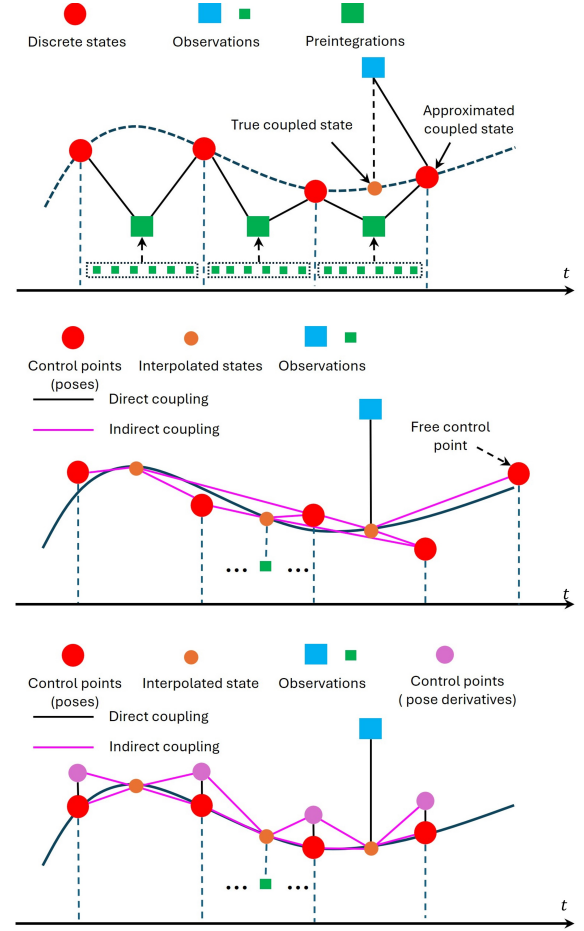


Fig. 1. Top: Discrete-time trajectory representation. Due to a finite number of represented states on the trajectory, we need to approximate, perform extra processing, or use sophisticated hardware synchronization to restrict the coupling of the observations with the state estimates. Middle vs Bottom: Comparison of B-spline and GP-based presentations of continuous time trajectory. While B-spline control points only consist of pseudo-poses that do not lie on the trajectory, GP control points extend the states to include the derivative states at each knot. Hence, the control points fully represent the states on the trajectory.

Besides, continuous-time trajectory representation also naturally allows the estimation of temporal offsets and querying the state at any time instance on the trajectory.

Several continuous-time approaches have been proposed over the years. The simplest of which is the linear-interpolation (LI) representation that assumes linear change between two consecutive poses [1]–[5]. However LI representation cannot represent derivative states, hence they could not fuse IMU data

directly at their timestamp. By using a smooth polynomial representation, B-spline can overcome the limitation of the LI model and has been extensively applied in the batch-optimization problems for multi-sensor calibration [6]–[8]. In recent years, B-spline has also been used for sliding-window-based CTME of visual(-inertial) odometry (VO / VIO) [9]–[12], UWB-IMU [13], and LiDAR(-inertial) odometry (LO / LIO) [14]–[17]. However, we find that B-spline representation still has some limitations. First, the B-spline model assumes that the trajectory follows a polynomial model. Indeed, in *motion planning*, user can choose a polynomial as the trajectory, but when estimating the motion, we cannot assume that the trajectory must follow a specific model. A simple counter-example is the velocity of a falling object under air drag, $\mathbf{v}(t) = \mathbf{v}_{\text{terminal}} \times \tanh(\mathbf{g} \cdot t / \mathbf{v}_{\text{terminal}})$, which follows an exponential trajectory, instead of polynomial. Second, because of the polynomial kinematic constraints, the control points are not actual states on the trajectory, which makes the initialization of new control points awkward. Finally, the B-spline also requires several control points that extend beyond the end time of the trajectory, which can move freely and make the regression problem ill-posed.

Due to the aforementioned issues, we find the Gaussian Process (GP) an appealing alternative. Rather than arbitrarily assuming some type of kinematics, GP uses an accurate state *transition model* as the prior, and only assumes the derivative of the highest-order to be a Gaussian-distributed stochastic term. Based on the order of the derivative, we can refer to the GP model as *random velocity*, *random acceleration*, or *random jerk*, etc. As illustrated in Fig. 1, while B-spline encodes the information on velocity and acceleration via a sequence of *control poses* under the interpolation rule, GP directly includes extra states for velocity, acceleration at each control points.

GP-based trajectory representation offers several advantages compared to B-spline. Apparently, while retaining all the benefits of the B-spline approach, GP representation also avoids the issue of free control points. In addition, as the GP control points are true states on the trajectory; initialization of new control points can be done easily with the state transition model. Moreover, the state interpolation process only involves the two adjacent control points, making the organization, query, and extension of the trajectory much more straightforward than in B-spline representation. Another advantage of GP model is that we can incorporate the covariance into the representation, which can also be propagated and interpolated just like the states.

Despite the aforementioned advantages, GP has a disadvantage in that the higher the order of the *rotational derivatives*, the more complex their closed forms kinematics become (we will elaborate on this in Sec. II-E). Due to this complexity, existing works only consider a second-order (random acceleration) model [18], or an approximated third-order (random jerk) model [19] in the rotational states. To the best of our knowledge, there is no general way to switch from one GP model to another with a higher order of derivative. In this paper, we show how the close forms of higher-order derivatives and their Jacobians can be theoretically obtained from the basic rules of calculus, which allows one to, in principle,

extend the GP formulation to any higher-order cases.

Another issue that comes to our attention is that few works have explored GP as a CTME approach. The most notable existing open-sourced work to be mentioned is STEAM¹, which have been adopted in [20]–[23]. However, we note that STEAM is a comprehensive library that covers many aspects of CTME, such as SO(3), SE(3) implementation, Gaussian-Newton solver, and CT trajectory management, etc. Though powerful, we believe that such a full-fledged engine could be harder to adopt due to compatibility issues. Another example of open-source GP representation is ESGPR [24]. However, ESGPR only considers the calibration applications, where a 9DOF vector-space GP is used to model the linear position, velocity, and acceleration states of a target. Thus, to further bolster the interest in GP-based CTME, we propose a new implementation named GPTR, featuring a GP trajectory representation for SE(3) states and their derivatives. The library only consists of a few C++ header files, requires only common dependencies such as Sophus² and Eigen³, and can be easily imported to other projects. Moreover, we also provide some minimal working examples of CTME with GPTR in various Maximum Likelihood Estimation (MLE) and Maximum A Posteriori (MAP) optimization schemes involving LiDAR, IMU, UWB, and visual factors, leveraging the popular Ceres Solver [25] with analytical Jacobians. These practical implementation approaches have been carefully deliberated to ensure ease of adoption by the community.

The contribution of our work can be stated as follows:

- We provide closed-form derivation of third-order GP trajectory representation and continuous-time motion estimation for SE(3) states and their derivatives.
- We release our source code for the benefit of the community. Notably, our GP framework is implemented as a header-only library, which can be easily integrated into other ME tasks.
- We develop several working examples of various MLE and MAP optimization problems with visual, UWB, IMU, and LiDAR factors, easily modified for other applications.

The remainder of this paper is organized as follows: Sec. II recalls the basic theory of motion estimation based on the Gaussian Process, i.e. propagation, interpolation, regression; Sec. III details several MAP optimization schemes leveraging image, IMU, UWB, and LiDAR measurements; Sec. IV presents the experiment results that showcase the capability of GPTR in these scenarios. Finally, Sec. V concludes the paper.

II. PRELIMINARIES

In this section, we will define the necessary notations and then lay out the theoretical foundations for employing the Gaussian Process in motion estimation.

A. Notations

In this paper, a matrix is denoted by a bold uppercase letter, and vectors with a bold lowercase letter. For a matrix **A**

¹<https://github.com/utiasASRL/steam>

²<https://github.com/strasdat/Sophus>

³<https://eigen.tuxfamily.org/>

(and similarly, for vectors), \mathbf{A}^\top denotes its transpose. Given $\mathbf{A} \in \mathbb{R}^{m \times n}$, we also write $\mathbf{A} = [a_{ij}]$, where a_{ij} refers to the entry at i -th row and j -th column, where $i = 0, \dots, m-1$ and $j = 0, \dots, n-1$. For two matrices $\mathbf{A} \in \mathbb{R}^{a \times b}$ and $\mathbf{B} \in \mathbb{R}^{c \times d}$, $\mathbf{A} \otimes \mathbf{B} \in \mathbb{R}^{ac \times bd}$ denotes their Kronecker product. For a number of square matrices $\{\mathbf{A}_i\}$ (including scalars), $\text{diag}(\dots \mathbf{A}_i \dots)$ denotes the block-diagonal matrix constructed from $\{\mathbf{A}_i\}$. Similarly, for $\{\mathbf{A}_i \in \mathbb{R}^3\}$, we denote $\text{vstack}(\dots \mathbf{A}_i \dots) \triangleq [\dots \mathbf{A}_i^\top \dots]^\top$.

In this paper, to avoid ambiguity, we may attach a left superscript to indicate the *parent* coordinate frame, and a left subscript for the *child* frame. Thus, ${}^{\mathbb{W}}\mathbf{R}_{\mathbb{B}}$ denotes the orientation of the frame \mathbb{B} (body) w.r.t. the frame \mathbb{W} (world). Moreover, for a vector \mathbf{v} , ${}^{\mathbb{B}}\mathbf{v}$, ${}^{\mathbb{W}}\mathbf{v}$ explicitly refer to the coordinates of \mathbf{v} in the coordinate frame \mathbb{B} and \mathbb{W} , respectively, and ${}^{\mathbb{W}}\mathbf{v} = {}^{\mathbb{W}}\mathbf{R}_{\mathbb{B}} {}^{\mathbb{B}}\mathbf{v}$. Similarly, we define a pose ${}^{\mathbb{W}}\mathbf{T}_{\mathbb{B}}$ as the tuple $({}^{\mathbb{W}}\mathbf{R}_{\mathbb{B}}, {}^{\mathbb{W}}\mathbf{p}_{\mathbb{B}})$, and the coordinate transform of a point \mathbf{x} is ${}^{\mathbb{W}}\mathbf{x} = {}^{\mathbb{W}}\mathbf{R}_{\mathbb{B}} {}^{\mathbb{B}}\mathbf{x} + {}^{\mathbb{W}}\mathbf{p}_{\mathbb{B}}$. When the frames are variable, to simplify notations we may supplant the full notation of the frame with the index or time stamp. For example ${}^{\mathbb{B}_i}\mathbf{T} = {}_i\mathbf{T}$ can denote the *extrinsics* of the sensor \mathbb{S}_i in the body frame. For a vector $\mathbf{x} \in \mathbb{R}^3$, \mathbf{x}^\times denotes the corresponding skew-symmetric matrix. We will also invoke the mapping $\text{Exp}(\cdot) : \mathbb{R}^3 \rightarrow \text{SO}(3)$ and its inverse $\text{Log}(\cdot) : \text{SO}(3) \rightarrow \mathbb{R}^3$.

$\mathcal{N}(\boldsymbol{\mu}, \boldsymbol{\Sigma})$ denotes a multivariate normal distribution with mean $\boldsymbol{\mu}$ and covariance $\boldsymbol{\Sigma}$, and $\mathcal{GP}(\boldsymbol{\mu}, \kappa)$ denotes a Gaussian Process with mean $\boldsymbol{\mu}$ and covariance κ .

B. GP Propagation

Denote $\mathbf{x}(t)$ as a state vector of interest. Let us assume that $\mathbf{x}(t)$ evolves by the following stochastic linear time-varying (LTV) system:

$$\dot{\mathbf{x}}(t) = \mathbf{A}(t)\mathbf{x}(t) + \mathbf{B}(t)\mathbf{w}(t), \quad \mathbf{w}(t) \sim \mathcal{N}(0, \boldsymbol{\Sigma}). \quad (1)$$

Also, we define $\Phi(t, t_0)$ as the state transition matrix of the deterministic system:

$$\dot{\mathbf{x}}(t) = \mathbf{A}(t)\mathbf{x}(t), \quad \mathbf{x}(t_0) = \mathbf{x}_0. \quad (2)$$

From (1) we have $\mathbf{x}(t) \sim \mathcal{GP}(\boldsymbol{\mu}(t), \boldsymbol{\kappa}(t, t'))$ with the *mean* and *covariance functions* $\boldsymbol{\mu}(t)$ and $\boldsymbol{\kappa}(t, t')$ defined as:

$$\begin{aligned} \boldsymbol{\mu}(t) &= \Phi(t, t_0)\boldsymbol{\mu}(t_0) \\ \boldsymbol{\kappa}(t, t_0) &= \Phi(t, t_0)\boldsymbol{\kappa}(t_0, t_0)\Phi(t, t_0)^\top + \mathbf{Q}(t, t_0) \\ \mathbf{Q}(t, t_0) &= \int_{t_0}^t \Phi(t, s)\mathbf{B}(s)\boldsymbol{\Sigma}\mathbf{B}(s)^\top \Phi(t, s)^\top ds. \end{aligned} \quad (3)$$

C. GP Interpolation

Given the samples of $\boldsymbol{\mu}(t)$ at different times $\{\boldsymbol{\mu}_k = \boldsymbol{\mu}(t_k)\}_{k=0,1,\dots,K}$, and assume that $\mathbf{x}(t)$ evolves according to (1), in [26], Barfoot et al. shows that the mean state at τ , for $\tau \in [t_k, t_{k+1})$, can be found by:

$$\boldsymbol{\mu}(\tau) = \boldsymbol{\Lambda}(\tau)\boldsymbol{\mu}_k + \boldsymbol{\Psi}(\tau)\boldsymbol{\mu}_{k+1}, \quad (4)$$

where $\boldsymbol{\Lambda}(\tau)$ and $\boldsymbol{\Psi}(\tau)$ are the mixer matrices that are defined as:

$$\boldsymbol{\Lambda}(\tau) = \Phi(\tau, t_k) - \boldsymbol{\Psi}(\tau)\Phi(t_{k+1}, t_k), \quad (5)$$

$$\boldsymbol{\Psi}(\tau) = \mathbf{Q}(\tau, t_k)\Phi(t_{k+1}, \tau)^\top \mathbf{Q}(t_{k+1}, t_k)^{-1}. \quad (6)$$

D. GP on Vector Space

For $\boldsymbol{\nu}(t) = (\mathbf{p}(t), \mathbf{v}(t), \mathbf{a}(t))$, where \mathbf{p} , \mathbf{v} , \mathbf{a} are the position, velocity, and acceleration, and assume a random *jerk* model, we have a GP based on the following linear time-invariant (LTI) system:

$$\dot{\boldsymbol{\nu}}(t) = \mathbf{A}\boldsymbol{\nu}(t) + \mathbf{B}\mathbf{w}_{\boldsymbol{\nu}}(t), \quad \mathbf{w}_{\boldsymbol{\nu}}(t) \sim \mathcal{N}(0, \boldsymbol{\Sigma}_{\boldsymbol{\nu}}), \quad (7)$$

$$\text{where } \mathbf{A} \triangleq \begin{bmatrix} \mathbf{0} & \mathbf{I} & \mathbf{0} \\ \mathbf{0} & \mathbf{0} & \mathbf{I} \\ \mathbf{0} & \mathbf{0} & \mathbf{0} \end{bmatrix}, \quad \mathbf{B} \triangleq \begin{bmatrix} \mathbf{0} \\ \mathbf{0} \\ \mathbf{I} \end{bmatrix}.$$

Let us define the transition matrix and the covariance matrix as follows:

$$\mathbf{F}(\Delta t) \triangleq \Phi(\Delta t, 0) = e^{\mathbf{A}\Delta t} \quad (8)$$

$$\mathbf{Q}_{\boldsymbol{\nu}}(\Delta t, \boldsymbol{\Sigma}_{\boldsymbol{\nu}}) \triangleq \int_0^{\Delta t} \mathbf{F}(s)\mathbf{B}\boldsymbol{\Sigma}_{\boldsymbol{\nu}}\mathbf{B}^\top \mathbf{F}(s)^\top ds, \quad (9)$$

Hence we can obtain discrete model:

$$\boldsymbol{\nu}_{k+1} = \mathbf{F}(\Delta t)\boldsymbol{\nu}_k + \boldsymbol{\eta}_k, \quad \boldsymbol{\eta}_k \sim \mathcal{N}(\mathbf{0}, \mathbf{Q}_{\boldsymbol{\nu}}(\Delta t, \boldsymbol{\Sigma}_{\boldsymbol{\nu}})), \quad (10)$$

where $\mathbf{F}(\Delta t)$ and $\mathbf{Q}_{\boldsymbol{\nu}}(\Delta t, \boldsymbol{\Sigma}_{\boldsymbol{\nu}})$ can be quickly calculated by the following formulas:

$$\begin{aligned} \mathbf{F}(\Delta t) &= [f_{nm}] \otimes \mathbf{I}; \quad \mathbf{Q}_{\boldsymbol{\nu}}(\Delta t, \boldsymbol{\Sigma}_{\boldsymbol{\nu}}) = [q_{nm}] \otimes \boldsymbol{\Sigma}_{\boldsymbol{\nu}}; \\ f_{nm} &= \begin{cases} \Delta t^m/m!, & \text{if } m \geq n \\ 0, & \text{otherwise} \end{cases}; \\ q_{nm} &= \frac{\Delta t^{2D+1-n-m}}{(2D+1-n-m)(D-n)!(D-m)!}; \\ D &= N-1; \quad n, m \in \{0, \dots, N-1\}, \Delta t = t - t_0. \end{aligned} \quad (11)$$

where N is the order of the system, which, for the specific case of $N = 3$, we have \mathbf{F} and \mathbf{Q} as:

$$\mathbf{F}(\Delta t) = \begin{bmatrix} \mathbf{I} & \Delta t \mathbf{I} & 0.5 \Delta t^2 \mathbf{I} \\ \mathbf{0} & \mathbf{I} & \Delta t \mathbf{I} \\ \mathbf{0} & \mathbf{0} & \mathbf{I} \end{bmatrix}, \quad (12)$$

$$\mathbf{Q}(\Delta t, \boldsymbol{\Sigma}_{\boldsymbol{\nu}}) = \begin{bmatrix} \frac{\Delta t^5}{20} \boldsymbol{\Sigma}_{\boldsymbol{\nu}} & \frac{\Delta t^4}{8} \boldsymbol{\Sigma}_{\boldsymbol{\nu}} & \frac{\Delta t^3}{6} \boldsymbol{\Sigma}_{\boldsymbol{\nu}} \\ \frac{\Delta t^4}{8} \boldsymbol{\Sigma}_{\boldsymbol{\nu}} & \frac{\Delta t^3}{2} \boldsymbol{\Sigma}_{\boldsymbol{\nu}} & \frac{\Delta t^2}{2} \boldsymbol{\Sigma}_{\boldsymbol{\nu}} \\ \frac{\Delta t^3}{6} \boldsymbol{\Sigma}_{\boldsymbol{\nu}} & \frac{\Delta t^2}{2} \boldsymbol{\Sigma}_{\boldsymbol{\nu}} & \Delta t \boldsymbol{\Sigma}_{\boldsymbol{\nu}} \end{bmatrix}, \quad (13)$$

Remark 1. The explicit forms of \mathbf{F} and \mathbf{Q} in (12) for some specific order have been frequently presented in the existing literature on GP [18], [19], [24], [26]. In this paper, we stipulate the general formulas (11) that can generate \mathbf{F} , \mathbf{Q} to any white-noise-on-(N -th-derivative) model.

E. GP on Manifold

Let us define the state $\boldsymbol{\rho}(t) = (\mathbf{R}(t), \boldsymbol{\omega}(t), \boldsymbol{\alpha}(t)) \in \text{SO}(3) \times \mathbb{R}^3 \times \mathbb{R}^3$, where $\mathbf{R}(t)$, $\boldsymbol{\omega}(t)$, $\boldsymbol{\alpha}(t)$ are respectively the rotation, angular velocity, and angular acceleration states. The evolution of $\boldsymbol{\rho}(t)$ can be modelled by the following process:

$$\dot{\mathbf{R}}(t) = \mathbf{R}(t)\boldsymbol{\omega}(t)^\times, \quad (14)$$

$$\dot{\boldsymbol{\omega}}(t) = \boldsymbol{\alpha}(t), \quad (15)$$

$$\dot{\boldsymbol{\alpha}}(t) \sim \mathcal{N}(0, \boldsymbol{\Sigma}_{\boldsymbol{\rho}}). \quad (16)$$

However, (14) is nonlinear, and no closed-form solution of the mean and covariance of this process is known to the best of our knowledge. To resolve this issue, Tang et al. [19] proposed a different parameterization based on the rotation vector. Specifically, for each interval $[t_k, t_{k+1})$ we define the *local states* $\theta(t)$ and $\gamma(t)$ as follows:

$$\theta(t) \triangleq \text{Log}(\mathbf{R}_k^{-1} \mathbf{R}(t)), \quad (17)$$

$$\gamma(t) = [\theta(t)^\top, \dot{\theta}(t)^\top, \ddot{\theta}(t)^\top]^\top, \quad (18)$$

which belong to a vector space, and we can assume $\gamma(t)$ evolves by the same system as (7):

$$\dot{\gamma}(t) = \mathbf{A}\gamma(t) + \mathbf{B}\mathbf{w}_\gamma(t), \quad \mathbf{w}_\gamma(t) \sim \mathcal{N}(0, \Sigma_\gamma). \quad (19)$$

By the model (19), propagation and interpolation of the rotation state and its derivatives can be performed on flat Euclidean space $\mathbb{R}^3 \times \mathbb{R}^3 \times \mathbb{R}^3$ just like (7). Based on (18), we find the following mappings to convert between $\gamma(t)$ and $\rho(t)$ as follows:

$$\begin{aligned} \mathbf{R} &= \mathbf{R}_0 \text{Exp}(\theta), \\ \omega &= \frac{\partial}{\partial \theta} [\mathbf{R}_0 \text{Exp}(\theta)] \frac{d\theta}{dt} \triangleq J_r(\theta) \dot{\theta}, \\ \alpha &= \frac{d\omega}{dt} = J_r(\theta) \frac{d\dot{\theta}}{dt} + \frac{\partial}{\partial \theta} [J_r(\theta) \dot{\theta}] \frac{d\theta}{dt} \\ &\triangleq J_r(\theta) \ddot{\theta} + H_\theta(\theta, \dot{\theta}) \dot{\theta}, \\ \theta &= \text{Log}(\mathbf{R}_0^{-1} \mathbf{R}), \\ \dot{\theta} &= J_r^{-1}(\theta) \omega, \\ \ddot{\theta} &= \frac{d\dot{\theta}}{dt} = J_r^{-1}(\theta) \frac{d\omega}{dt} + \frac{\partial}{\partial \theta} [J_r^{-1}(\theta) \omega] \frac{d\theta}{dt}, \\ &\triangleq J_r^{-1}(\theta) \alpha + H'_\theta(\theta, \omega) \dot{\theta}, \end{aligned} \quad (20)$$

where J_r is the *right Jacobian* of $\text{SO}(3)$ and J_r^{-1} is its *inverse*; and $H_\theta(\theta, \dot{\theta})$, $H'_\theta(\theta, \omega)$ are detailed in Appendix A.

Remark 2. Tang et al. [19] simplified the above mappings by the Taylor expansion. In our paper the closed forms of these mappings are found analytically by appropriately applying the chain rule and the product rules in the calculation of $\frac{\partial}{\partial \theta} [J_r(\theta) \dot{\theta}]$ and $\frac{\partial}{\partial \theta} [J_r^{-1}(\theta) \omega]$, as detailed in the Appendices A.

F. GP-based Continuous-Time Trajectory Regression

1) *Trajectory Representation:* A continuous-time trajectory represented by GP can be defined by three sets of user-defined parameters:

- The knot length $\Delta t \in \mathbb{R}^+$.
- A set of control points $\{\hat{\mathcal{X}}_k\}_{k=0}^K$, where $\hat{\mathcal{X}}_k \triangleq (\hat{\mathbf{R}}_k, \hat{\omega}_k, \hat{\alpha}_k, \hat{\mathbf{p}}_k, \hat{\mathbf{v}}_k, \hat{\mathbf{a}}_k) \in \text{SO}(3) \times \mathbb{R}^3 \times \mathbb{R}^3 \times \mathbb{R}^3 \times \mathbb{R}^3 \times \mathbb{R}^3$. Each control point represents the state estimates of the robot at the *knot* $t_k = t_0 + k\Delta t$.
- The covariance matrices $\Sigma_\nu, \Sigma_\gamma \in \mathbb{R}^{3 \times 3}$ as defined in (7) and (19).

With this representation, the robot's state at each time instance in $[t_0, t_K]$ can be found by the interpolation (4). We assume that the *rotational states* $\rho_k = (\mathbf{R}_k, \omega_k, \alpha_k)$ evolve by

the model (19), and the translational states $\nu_k = (\mathbf{p}_k, \mathbf{v}_k, \mathbf{a}_k)$ follow (7).

2) *Regression:* Given an observation or sensor measurement \mathcal{Z} that is coupled with the state \mathcal{X}_t via some observation model $h(\mathcal{Z}, \mathcal{X}_t, \dots, \eta) = 0$, where η represents the noise or uncertainty. The regression problem can be formalized as:

$$\text{argmin}_{\{\hat{\mathcal{X}}_m\}_{m=0}^K} \sum_{\mathcal{Z}} \|r(\mathcal{Z}, \hat{\mathcal{X}}_t, \dots)\|_{\mathbf{W}}^2, \quad (21)$$

where $\|r\|_{\mathbf{W}}^2 \triangleq r^\top \mathbf{W} r$, and $r \triangleq h(\mathcal{Z}, \hat{\mathcal{X}}_t, \dots, \eta)|_{\eta=0}$ is the residual and \mathbf{W} is a weight based on the inverse of the covariance of η (also known as the information matrix). Crucial to the solving of (21), one needs to calculate the Jacobian of the residual $r(\mathcal{Z}, \hat{\mathcal{X}}_t, \dots)$ over the states estimate $\hat{\mathcal{X}}_a, \hat{\mathcal{X}}_b$ where $[t_a, t_b] \ni t$. By using the chain rule, we have

$$\frac{\partial r}{\partial \hat{\mathcal{X}}_a} = \frac{\partial r}{\partial \hat{\mathcal{X}}_t} \frac{\partial \hat{\mathcal{X}}_t}{\partial \hat{\mathcal{X}}_a}, \quad \frac{\partial r}{\partial \hat{\mathcal{X}}_b} = \frac{\partial r}{\partial \hat{\mathcal{X}}_t} \frac{\partial \hat{\mathcal{X}}_t}{\partial \hat{\mathcal{X}}_b}. \quad (22)$$

The Jacobian $\frac{\partial r}{\partial \hat{\mathcal{X}}_t}$ depends on each specific residuals. However, the Jacobians $\frac{\partial \hat{\mathcal{X}}_t}{\partial \hat{\mathcal{X}}_a}$ and $\frac{\partial \hat{\mathcal{X}}_t}{\partial \hat{\mathcal{X}}_b}$ always follow specific formulas. With the choice of third-order GP in both rotational (19) and translational states (7), the calculations of these Jacobians can be quite involved, especially for the rotational states. However, they can still be calculated by following the basic rules of calculus, and we provide a systematic procedure for these calculations in Appendix B. Also, it should be noted that there can be other states $\mathcal{X}_{t_1}, \mathcal{X}_{t_2}, \dots$ coupled with \mathcal{Z} in $h(\cdot)$. However, the calculation of Jacobian is the same for all of these states.

III. GP-BASED CTME SCENARIOS

In this section, we will present some examples of GPTR in different CTME scenarios. Sections III-A, III-B, III-C will present the general formulation of these CTME schemes for visual, ranging, and LiDAR scenarios, then the details of the factors are elaborated in Section III-D.

A. Visual-Inertial Motion Estimation and Calibration

In this first example, we demonstrate the application of GPTR in calibrating visual-inertial sensor suites. Let us define the state estimates as follows:

$$\hat{\mathcal{T}} \triangleq (\dots, \hat{\mathcal{X}}_m, \dots, \hat{\mathbf{b}}_a, \hat{\mathbf{b}}_\omega, \hat{\mathbf{g}}, \hat{\mathbf{c}}_0^\top \hat{\mathbf{T}}, \hat{\mathbf{c}}_1^\top \hat{\mathbf{T}}), \quad (23)$$

$$\hat{\mathcal{X}}_m = (\hat{\mathbf{R}}_m, \hat{\omega}_m, \hat{\alpha}_m, \hat{\mathbf{p}}_m, \hat{\mathbf{v}}_m, \hat{\mathbf{a}}_m), \quad (24)$$

where $\hat{\mathbf{b}}_a$ and $\hat{\mathbf{b}}_\omega$ are accelerometer and gyroscope biases, respectively. $\hat{\mathcal{X}}_m$ are the control points of the trajectory estimate of the IMU sensor. $\hat{\mathbf{g}}$ denotes the estimated gravity vector. $\{\hat{\mathbf{c}}_i^\top \hat{\mathbf{T}}\}_{i=0}^1 \triangleq \{(\hat{\mathbf{c}}_i^\top \hat{\mathbf{R}}_i, \hat{\mathbf{c}}_i^\top \hat{\mathbf{p}}_i)\}_{i=0}^1$ are the transformation from camera i to IMU frame, i.e., the extrinsics. Hence, the motion estimation and calibration using known landmarks in a batch-wise manner is formulated as the minimization of the following cost function:

$$f(\hat{\mathcal{T}}) = \sum_{(\hat{\mathcal{X}}_k, \hat{\mathcal{X}}_{k+1})} \|r_{\mathcal{M}}\|_{\mathbf{W}_{\mathcal{M}}}^2 + \sum_{\mathcal{C}_t} \|r_{\mathcal{C}}\|_{\mathbf{W}_{\mathcal{C}}}^2 + \sum_{\mathcal{I}_t} \|r_{\mathcal{I}}\|_{\mathbf{W}_{\mathcal{I}}}^2, \quad (25)$$

where $r_{\mathcal{M}}$, $r_{\mathcal{C}}$, and $r_{\mathcal{I}}$ are the *motion prior*, projection, and IMU residuals, respectively. $\mathbf{W}_{\mathcal{M}}$, $\mathbf{W}_{\mathcal{C}}$, and $\mathbf{W}_{\mathcal{I}}$ are the corresponding information matrices (inverse of covariance). \mathcal{C}_t and \mathcal{I}_t refer to the visual and inertial observations obtained during the optimization period, which will be elaborated in Sec. III-D.

B. UWB-Inertial Estimation

Next, we demonstrate a sliding-window sensor fusion scheme for IMU measurement and time-difference-of-arrival (TDoA) range measurements with GPTR. Specifically, we aim to estimate the following states on a sliding window:

$$\hat{\mathcal{T}} \triangleq (\dots, \hat{\mathcal{X}}_m, \dots, \hat{\mathbf{b}}_a, \hat{\mathbf{b}}_\omega), \quad (26)$$

with IMU biases $\hat{\mathbf{b}}_a$, $\hat{\mathbf{b}}_\omega$ and control point $\hat{\mathcal{X}}_m$ the same as defined in (23) and (24). The problem formulation for this scenario becomes minimizing the following cost function:

$$\begin{aligned} f(\hat{\mathcal{T}}) = & \|r_{\mathcal{P}}\|_{\mathbf{W}_{\mathcal{P}}}^2 + \sum_{(\hat{\mathcal{X}}_k, \hat{\mathcal{X}}_{k+1})} \|r_{\mathcal{M}}\|_{\mathbf{W}_{\mathcal{M}}}^2 \\ & + \sum_{\mathcal{U}_t} \|r_{\mathcal{U}}\|_{\mathbf{W}_{\mathcal{U}}}^2 + \sum_{\mathcal{I}_t} \|r_{\mathcal{I}}\|_{\mathbf{W}_{\mathcal{I}}}^2, \end{aligned} \quad (27)$$

where $r_{\mathcal{P}}$ is the prior residual term from marginalization. $r_{\mathcal{M}}$, $r_{\mathcal{U}}$, and $r_{\mathcal{I}}$ denote the motion prior, UWB, and IMU residuals, respectively. $\mathbf{W}_{\mathcal{P}}$, $\mathbf{W}_{\mathcal{M}}$, $\mathbf{W}_{\mathcal{U}}$, and $\mathbf{W}_{\mathcal{I}}$ are the corresponding information matrices. \mathcal{U}_t and \mathcal{I}_t are the UWB and IMU observations within the sliding window.

C. Multi-LiDAR Coupled-Motion Estimation

In the previous scenarios, only one trajectory was represented by the GP. Inspired by [24], we also demonstrate the use of GPTR in a GP-based multi-trajectory optimization scheme. Different from [24], which performed batch optimization for sensors with overlapping field of view (FOV). In this paper, we shall investigate a Maximum A Posteriori (MAP) estimation scheme of two LiDARs that do not have any overlapping FOV. Moreover, while motion distortion is often considered undesirable in discrete-time motion estimation schemes, in this example, we would also like to demonstrate that CTME with GP representation can directly extract the motion in the LiDAR distortion *without relying on IMU*. Specifically, we define the following state estimates on a sliding window:

$$\hat{\mathcal{T}} \triangleq (\dots, \hat{\mathcal{X}}_m, \dots, \hat{\mathcal{X}}_{k+1}, \dots, \hat{\mathbf{L}}_0, \hat{\mathbf{L}}_1), \quad (28)$$

$$_i \hat{\mathcal{X}}_m = (_i \hat{\mathbf{R}}_m, _i \hat{\omega}_m, _i \hat{\alpha}_m, _i \hat{\mathbf{p}}_m, _i \hat{\mathbf{v}}_m, _i \hat{\mathbf{a}}_m), \quad (29)$$

where $_i \hat{\mathcal{X}}_m$ are the control points on the sliding window of trajectory i and $\hat{\mathbf{L}}_0, \hat{\mathbf{L}}_1 \triangleq (_0 \mathbf{R}, _0 \mathbf{p}) \in \text{SE}(3)$ are the transformations between LiDAR 0 and LiDAR 1. The state estimates can be optimized via the cost function (30):

$$\begin{aligned} f(\hat{\mathcal{T}}) = & \|r_{\mathcal{P}}\|_{\mathbf{W}_{\mathcal{P}}}^2 + \sum_{(\hat{\mathcal{X}}_k, \hat{\mathcal{X}}_{k+1})} \|r_{\mathcal{M}}\|_{\mathbf{W}_{\mathcal{M}}}^2 \\ & + \sum_{\mathcal{L}_t} \|r_{\mathcal{L}}\|_{\mathbf{W}_{\mathcal{L}}}^2 + \sum_{\tau} \|r_{\mathcal{E}}\|_{\mathbf{W}_{\mathcal{E}}}^2, \end{aligned} \quad (30)$$

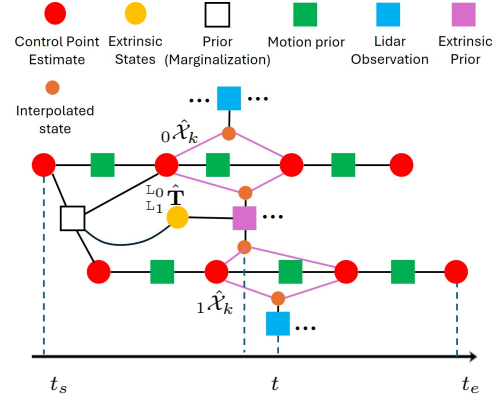


Fig. 2. The factor graph of the GP-based multi-LiDAR coupled-motion estimation scheme. We have two trajectories corresponding to two LiDARs. Each square represents one factor, and the lines indicate the coupled states. The detail of each factor is given in Sec. III-D.

where $r_{\mathcal{P}}$, $r_{\mathcal{M}}$ are respectively the prior from marginalization and the motion prior, $r_{\mathcal{L}}$ is the residual of LiDAR-based point-to-plane factors, and $r_{\mathcal{E}}$ the residual of *extrinsic prior factor*. $\mathbf{W}_{\mathcal{P}}$, $\mathbf{W}_{\mathcal{M}}$, $\mathbf{W}_{\mathcal{L}}$, $\mathbf{W}_{\mathcal{E}}$ are correspondingly their information matrices. Fig. 2 illustrates the factor graph based on this cost function with two LiDARs.

D. Factors

In this section, we shall elaborate on the factors presented in the previous CTME schemes. Specifically, for each factor, we will discuss the observation \mathcal{Z} , its residual $r_{\mathcal{Z}}$, the weight $\mathbf{W}_{\mathcal{Z}}$, and the Jacobian of the $r_{\mathcal{Z}}$ w.r.t. to the interpolated states.

1) *Visual factor*: Each visual factor is constructed from a visual observation $\mathcal{C}_t \triangleq ({}^w \mathbf{l}, z_c)$, where ${}^w \mathbf{l}$ is the coordinate in the world frame of the landmark \mathbf{l} , and $z_c \in \mathbb{R}^2$ is the coordinate of \mathbf{l} in the image at timestamp t . The projection factor is defined as follows:

$$r_{\mathcal{C}} = \pi({}^{c_i} \hat{\mathbf{l}}) - z_c, \quad \mathbf{W}_{\mathcal{C}} = \text{diag}(w_{c_1}, w_{c_2}), \quad \text{with} \quad (31)$$

$${}^{c_i} \hat{\mathbf{l}} = {}_{c_i}^{\mathbf{I}} \hat{\mathbf{R}}^{\top} \left({}^{\mathbf{I}} \hat{\mathbf{l}} - {}_{c_i}^{\mathbf{I}} \hat{\mathbf{p}} \right), \quad {}^{\mathbf{I}} \hat{\mathbf{l}} = \hat{\mathbf{R}}^{\top}(t) ({}^w \mathbf{l} - \hat{\mathbf{p}}(t)), \quad (32)$$

where ${}^{\mathbf{I}} \hat{\mathbf{l}}$ denotes the landmark's coordinate in the IMU frame, obtained via the interpolated pose $(\hat{\mathbf{R}}(t), \hat{\mathbf{p}}(t))$, and ${}^{c_i} \hat{\mathbf{l}}$ is its coordinate in the camera frame obtained via the transformation $({}_{c_i}^{\mathbf{I}} \hat{\mathbf{R}}, {}_{c_i}^{\mathbf{I}} \hat{\mathbf{p}})$. The resulting position ${}^{c_i} \hat{\mathbf{l}}$ is then projected onto the image plane by the camera model-related function $\pi(\cdot)$.

The weight $\mathbf{W}_{\mathcal{C}}$ correlates with the noise on z_c , which is set as a diagonal matrix in our experiments. The Jacobians of the residual $r_{\mathcal{C}}$ w.r.t. the interpolated pose are

$$\mathbf{J}_{\hat{\mathbf{R}}(t)}^{r_{\mathcal{C}}} = \mathbf{J}_{c_i \hat{\mathbf{l}}}^{r_{\mathcal{C}}} \mathbf{J}_{i \hat{\mathbf{l}}}^{c_i \hat{\mathbf{l}}} \mathbf{J}_{\hat{\mathbf{R}}(t)}^{i \hat{\mathbf{l}}} \quad \text{and} \quad (33)$$

$$\mathbf{J}_{\hat{\mathbf{p}}(t)}^{r_{\mathcal{C}}} = \mathbf{J}_{c_i \hat{\mathbf{l}}}^{r_{\mathcal{C}}} \mathbf{J}_{i \hat{\mathbf{l}}}^{c_i \hat{\mathbf{l}}} \mathbf{J}_{\hat{\mathbf{p}}(t)}^{i \hat{\mathbf{l}}}, \quad (34)$$

where the first component of the above product depends on the camera projection model. For instance, if the projection function for pinhole camera model is $\pi([x, y, z]^{\top}) = [f_x \frac{x}{z} + c_x, f_y \frac{y}{z} + c_y]^{\top}$ as in VINS-Fusion [27], with f_x , f_y , c_x , and

c_y being camera intrinsic parameters, then $\mathbf{J}_{c_i \hat{\mathbf{l}}}^{rc}$ is derived as

$$\mathbf{J}_{c_i \hat{\mathbf{l}}}^{rc} = \begin{bmatrix} f_x \hat{l}_z^{-1} & 0 & -f_x \hat{l}_x \hat{l}_z^{-2} \\ 0 & f_y \hat{l}_z^{-1} & -f_y \hat{l}_y \hat{l}_z^{-2} \end{bmatrix}, \quad (35)$$

with $c_i \hat{\mathbf{l}} \triangleq [\hat{l}_x, \hat{l}_y, \hat{l}_z]^\top$. The remaining Jacobians are computed as follows:

$$\mathbf{J}_{i \hat{\mathbf{l}}}^{c_i} = {}^i \mathbf{R}^{c_i \top}, \quad \mathbf{J}_{\hat{\mathbf{R}}(t)}^{i \hat{\mathbf{l}}} = {}^i \hat{\mathbf{l}}^\times, \quad \text{and} \quad (36)$$

$$\mathbf{J}_{\hat{\mathbf{p}}(t)}^{i \hat{\mathbf{l}}} = -{}^i \mathbf{R}^{c_i \top} \hat{\mathbf{R}}^\top(t), \quad (37)$$

where ${}^i \hat{\mathbf{l}}^\times \in \mathbb{R}^{3 \times 3}$ denotes the skew-symmetric matrix. Similar to (33), the Jacobians w.r.t. the calibration parameters ${}^i \mathbf{R}$ and ${}^i \hat{\mathbf{p}}$ are derived as

$$\mathbf{J}_{i \hat{\mathbf{R}}}^{rc} = \mathbf{J}_{c_i \hat{\mathbf{l}}}^{rc} \mathbf{J}_{i \hat{\mathbf{l}}}^{c_i} \quad \text{and} \quad \mathbf{J}_{i \hat{\mathbf{p}}}^{rc} = \mathbf{J}_{c_i \hat{\mathbf{l}}}^{rc} \mathbf{J}_{i \hat{\mathbf{l}}}^{c_i} \hat{\mathbf{p}}, \quad \text{with} \quad (38)$$

$$\mathbf{J}_{i \hat{\mathbf{R}}}^{c_i} = c_i \hat{\mathbf{l}}^\times \quad \text{and} \quad \mathbf{J}_{i \hat{\mathbf{p}}}^{c_i} = -{}^i \mathbf{R}^{c_i \top}. \quad (39)$$

2) *UWB factor*: From the UWB sensor, we receive a TDoA observation $\mathcal{U}_t = (z_{\mathcal{U}}, {}^B \mathbf{x}, \mathbf{y}_i, \mathbf{y}_j)$, where $z_{\mathcal{U}}$ is the scalar TDoA measurement, ${}^B \mathbf{x}$ is the offset of the UWB tag w.r.t. the inertial body frame, and $\mathbf{y}_i, \mathbf{y}_j$ are the coordinates of the two anchors in the UWB frame. The TDoA UWB residual is therefore defined as follows:

$$r_{\mathcal{U}} = \|\mathbf{s}_{\text{tag}} - \mathbf{y}_i\| - \|\mathbf{s}_{\text{tag}} - \mathbf{y}_j\| - z_{\mathcal{U}}, \quad \mathbf{W}_{\mathcal{U}} \in \mathbb{R}^+, \quad (40)$$

where $\mathbf{s}_{\text{tag}} = \hat{\mathbf{R}}(t) {}^B \mathbf{x} + \hat{\mathbf{p}}(t)$.

The weight $\mathbf{W}_{\mathcal{U}}$ is set as a scalar that is proportional to the inverse of the noise on $z_{\mathcal{U}}$. The Jacobian of $r_{\mathcal{U}}$ w.r.t. the interpolated pose is derived as follows:

$$\mathbf{J}_{\hat{\mathbf{R}}(t)}^{r_{\mathcal{U}}} = -\mathbf{J}_{\mathbf{s}_{\text{tag}}}^{r_{\mathcal{U}}} \hat{\mathbf{R}}(t) {}^B \mathbf{x}^\times \quad \text{and} \quad \mathbf{J}_{\hat{\mathbf{p}}(t)}^{r_{\mathcal{U}}} = \mathbf{J}_{\mathbf{s}_{\text{tag}}}^{r_{\mathcal{U}}}, \quad \text{with} \quad (41)$$

$$\mathbf{J}_{\mathbf{s}_{\text{tag}}}^{r_{\mathcal{U}}} = \frac{\mathbf{s}_{\text{tag}}^\top - \mathbf{y}_i^\top}{\|\mathbf{s}_{\text{tag}} - \mathbf{y}_i\|} - \frac{\mathbf{s}_{\text{tag}}^\top - \mathbf{y}_j^\top}{\|\mathbf{s}_{\text{tag}} - \mathbf{y}_j\|}. \quad (42)$$

3) *IMU factor*: Given an IMU measurement consisting of angular velocity \mathbf{z}_ω and acceleration \mathbf{z}_a , we construct the following residual

$$r_{\mathcal{I}} = \begin{bmatrix} r_\omega \\ r_a \\ r_{b_\omega} \\ r_{b_a} \end{bmatrix} = \begin{bmatrix} \hat{\omega}(t) + \hat{\mathbf{b}}_\omega - \mathbf{z}_\omega \\ {}^i \hat{\mathbf{a}} + \hat{\mathbf{b}}_a - \mathbf{z}_a \\ \hat{\mathbf{b}}_\omega - \bar{\mathbf{b}}_\omega \\ \hat{\mathbf{b}}_a - \bar{\mathbf{b}}_a \end{bmatrix}, \quad \text{with} \quad (43)$$

$$\mathbf{W}_{\mathcal{I}} = \text{diag}(\mathbf{W}_\omega, \mathbf{W}_a, \mathbf{W}_{b_\omega}, \mathbf{W}_{b_a}). \quad (44)$$

r_ω is the gyroscope residual, where $\hat{\omega}(t)$ denotes the interpolated angular velocity from (20), and $\hat{\mathbf{b}}_\omega$ is the estimated gyroscope bias. r_a is the accelerometer residual, where the acceleration ${}^i \hat{\mathbf{a}} = \hat{\mathbf{R}}(t)^\top (\hat{\mathbf{a}}(t) + \hat{\mathbf{g}})$ is obtained by first transforming the interpolated acceleration $\hat{\mathbf{a}}(t)$ from the world frame by (4) together with gravity $\hat{\mathbf{g}}$ to the IMU frame using the interpolated orientation. $\hat{\mathbf{b}}_a$ denotes the estimated accelerometer bias. r_{b_ω} and r_{b_a} are the residuals of gyroscope and accelerometer biases, respectively. This indicates the changes in corresponding biases w.r.t. the estimates $\bar{\mathbf{b}}_\omega$ and $\bar{\mathbf{b}}_a$ from the last window. For a batch-wise optimization, residuals r_{b_ω} and r_{b_a} are disregarded.

The weight $\mathbf{W}_{\mathcal{I}}$ is simply a block diagonal matrix with each diagonal block corresponding to the inverse of the covariance of \mathbf{z}_ω , \mathbf{z}_a and changes in $\hat{\mathbf{b}}_\omega$ and $\hat{\mathbf{b}}_a$. The Jacobians of this residual w.r.t. each parameter are derived as follows.

$$\mathbf{J}_{\hat{\mathbf{R}}(t)}^{r_a} = {}^i \hat{\mathbf{a}}^\times, \quad \mathbf{J}_{\hat{\mathbf{a}}(t)}^{r_a} = \hat{\mathbf{R}}(t)^\top, \quad \mathbf{J}_{\hat{\mathbf{g}}}^{r_a} = \hat{\mathbf{R}}(t)^\top. \quad (45)$$

And the remaining Jacobians $\mathbf{J}_{\hat{\omega}(t)}^{r_\omega}$, $\mathbf{J}_{\hat{\mathbf{b}}_\omega}^{r_\omega}$, $\mathbf{J}_{\hat{\mathbf{b}}_a}^{r_a}$, $\mathbf{J}_{\hat{\mathbf{b}}_\omega}^{r_{b_\omega}}$, and $\mathbf{J}_{\hat{\mathbf{b}}_a}^{r_{b_a}}$ are all equal to \mathbf{I} .

Remark 3. Thanks to the continuous-time trajectory representation, the residual and Jacobians of the IMU factors become much simpler compared to the preintegration model in discrete-time formulation [28].

4) *LiDAR factor*: The LiDAR factor is created by associating the pointcloud with the map, and then the following residual is constructed from each point-to-plane association:

$$r_{\mathcal{L}} \triangleq \mathbf{n}^\top ({}_i \hat{\mathbf{R}}(t) {}^B(t) \check{\mathbf{f}} + {}_i \hat{\mathbf{p}}_t) + \mu, \quad \mathbf{W}_{\mathcal{L}} = w_{\mathcal{L}} \in \mathbb{R}^+, \quad (46)$$

where ${}^B(t) \check{\mathbf{f}} \in \mathbb{R}^3$ is the raw LiDAR point from the LiDAR scan, $\mu \in \mathbb{R}$, $\mathbf{n} \in \mathbb{R}^3$, $\|\mathbf{n}\| = 1$ are the coefficients of the plane that $\check{\mathbf{f}}$ is associated with.

$\mathbf{W}_{\mathcal{L}}$ is a scalar weight that is proportional to the noise from the LiDAR measurement and the association uncertainty. The Jacobian of $r_{\mathcal{L}}$ w.r.t. the interpolated pose $(\hat{\mathbf{R}}_t, \hat{\mathbf{p}}_t)$ is:

$$\mathbf{J}_{i \hat{\mathbf{R}}(t)}^{r_{\mathcal{L}}} = -\mathbf{n}^\top {}_i \hat{\mathbf{R}}(t) {}^B(t) \check{\mathbf{f}}^\times, \quad \mathbf{J}_{i \hat{\mathbf{p}}(t)}^{r_{\mathcal{L}}} = \mathbf{n}^\top. \quad (47)$$

5) *Motion prior*: In all previous examples, between every two consecutive control points \mathcal{X}_a and \mathcal{X}_b on the same trajectory (we denote $a = k$ and $b = k + 1$ for simpler notations), we add a motion prior factor with residual $r_{\mathcal{M}}$ and the weight $\mathbf{W}_{\mathcal{M}}$ as follows:

$$r_{\mathcal{M}} = \begin{bmatrix} r_\gamma \\ r_\nu \end{bmatrix} \triangleq \begin{bmatrix} \hat{\gamma}_b - \mathbf{F}(\Delta t) \hat{\gamma}_a \\ \hat{\nu}_b - \mathbf{F}(\Delta t) \hat{\nu}_a \end{bmatrix},$$

$$\mathbf{W}_{\mathcal{M}} = \begin{bmatrix} \mathbf{Q}_\gamma(\Delta t) & \mathbf{0} \\ \mathbf{0} & \mathbf{Q}_\nu(\Delta t) \end{bmatrix}^{-1}.$$

This factor is crucial for the convergence of CTME problem based on GP, as it constrains the feasible trajectories to those conforming to the dynamic models (7) and (19), effectively acting as a smoothing factor.

From (11), we can easily obtain the Jacobians of r_ν as

$$\begin{aligned} \mathbf{J}_{\hat{\mathbf{p}}_a}^{r_\nu} &= \text{vstack}(-\mathbf{I}, \mathbf{0}, \mathbf{0}), \\ \mathbf{J}_{\hat{\mathbf{v}}_a}^{r_\nu} &= \text{vstack}(\mathbf{0}, -\Delta t \mathbf{I}, -\mathbf{I}), \\ \mathbf{J}_{\hat{\mathbf{a}}_a}^{r_\nu} &= \text{vstack}(-0.5 \Delta t^2 \mathbf{I}, -\Delta t \mathbf{I}, -\mathbf{I}), \\ \mathbf{J}_{\hat{\mathbf{p}}_b}^{r_\nu} &= \text{vstack}(\mathbf{I}, \mathbf{0}, \mathbf{0}), \\ \mathbf{J}_{\hat{\mathbf{v}}_b}^{r_\nu} &= \text{vstack}(\mathbf{0}, \mathbf{I}, \mathbf{0}), \\ \mathbf{J}_{\hat{\mathbf{a}}_b}^{r_\nu} &= \text{vstack}(\mathbf{0}, \mathbf{0}, \mathbf{I}). \end{aligned}$$

The Jacobians of r_γ over the rotational states are more

complex, specifically:

$$\begin{aligned}
\mathbf{J}_{\hat{\mathbf{R}}_a}^{r_\gamma} &= \text{vstack}(\mathbf{J}_{\hat{\mathbf{R}}_a}^{\hat{\theta}_b}, \mathbf{J}_{\hat{\mathbf{R}}_a}^{\hat{\theta}_b}, \mathbf{J}_{\hat{\mathbf{R}}_a}^{\hat{\theta}_b}), \\
\mathbf{J}_{\hat{\omega}_a}^{r_\gamma} &= \text{vstack}(\mathbf{0}, -\Delta t \mathbf{I}, -\mathbf{I}), \\
\mathbf{J}_{\hat{\alpha}_a}^{r_\gamma} &= \text{vstack}(-0.5\Delta t^2 \mathbf{I}, -\Delta t \mathbf{I}, -\mathbf{I}), \\
\mathbf{J}_{\hat{\mathbf{R}}_b}^{r_\gamma} &= \text{vstack}(\mathbf{J}_{\hat{\mathbf{R}}_b}^{\hat{\theta}_b}, \mathbf{J}_{\hat{\mathbf{R}}_b}^{\hat{\theta}_b}, \mathbf{J}_{\hat{\mathbf{R}}_b}^{\hat{\theta}_b}), \\
\mathbf{J}_{\hat{\omega}_b}^{r_\gamma} &= \text{vstack}(\mathbf{0}, J_r^{-1}(\hat{\theta}_b), \mathbf{J}_{\hat{\omega}_b}^{\hat{\theta}_b}), \\
\mathbf{J}_{\hat{\alpha}_b}^{r_\gamma} &= \text{vstack}(\mathbf{0}, \mathbf{0}, J_r^{-1}(\hat{\theta}_b)),
\end{aligned}$$

where $\mathbf{J}_{\hat{\mathbf{R}}_a}^{\hat{\theta}_b}, \mathbf{J}_{\hat{\mathbf{R}}_a}^{\hat{\theta}_b}, \mathbf{J}_{\hat{\mathbf{R}}_a}^{\hat{\theta}_b}, \mathbf{J}_{\hat{\mathbf{R}}_b}^{\hat{\theta}_b}, \mathbf{J}_{\hat{\mathbf{R}}_b}^{\hat{\theta}_b}, \mathbf{J}_{\hat{\mathbf{R}}_b}^{\hat{\theta}_b}, J_r^{-1}(\hat{\theta}_b)$ are elaborated in the Appendix B.

6) *Extrinsic Prior Factor*: Since the two LiDARs are secured on the vehicle, we have the kinematic constraints ${}_1\mathbf{R}(t) = {}_0\mathbf{R}(t) \cdot {}_1\mathbf{R}$ and ${}_1\mathbf{p}(t) = {}_0\mathbf{p}(t) + {}_0\mathbf{R} \cdot {}_1\mathbf{p}(t)$ at any time instance. By taking derivatives on both sides, we can construct the following residuals:

$$r_{\mathcal{E}} = \text{vstack}(r_{\mathcal{E}_R}, r_{\mathcal{E}_\omega}, r_{\mathcal{E}_\alpha}, r_{\mathcal{E}_p}, r_{\mathcal{E}_v}, r_{\mathcal{E}_a}), \quad (48)$$

$$\mathbf{W}_{\mathcal{E}} = \begin{bmatrix} \mathbf{Q}_\gamma(\Delta t, \Sigma'_\gamma) & \mathbf{0} \\ \mathbf{0} & \mathbf{Q}'_\nu(\Delta t, \Sigma'_\nu) \end{bmatrix}^{-1}, \quad (49)$$

where $r_{\mathcal{E}_R}, r_{\mathcal{E}_\omega}, r_{\mathcal{E}_\alpha}, r_{\mathcal{E}_p}, r_{\mathcal{E}_v}, r_{\mathcal{E}_a}$ are defined as:

$$r_{\mathcal{E}_R} = \text{Log} \left[({}_0\hat{\mathbf{R}}(t) \cdot {}_1\hat{\mathbf{R}})^\top \cdot {}_1\hat{\mathbf{R}}(t) \right], \quad (50)$$

$$r_{\mathcal{E}_\omega} = {}_1\hat{\mathbf{R}} \cdot {}_1\hat{\omega}(t) - {}_0\hat{\omega}(t), \quad (51)$$

$$r_{\mathcal{E}_\alpha} = {}_1\hat{\mathbf{R}} \cdot {}_1\hat{\alpha}(t) - {}_0\hat{\alpha}(t), \quad (52)$$

$$r_{\mathcal{E}_p} = {}_1\hat{\mathbf{p}}(t) - {}_0\hat{\mathbf{p}}(t) - {}_0\hat{\mathbf{R}}(t) \cdot {}_1\hat{\mathbf{p}}, \quad (53)$$

$$r_{\mathcal{E}_v} = {}_1\hat{\mathbf{v}}(t) - {}_0\hat{\mathbf{v}}(t) - {}_0\hat{\mathbf{R}}(t) \cdot {}_0\hat{\omega}(t)^\times \cdot {}_1\hat{\mathbf{p}}, \quad (54)$$

$$r_{\mathcal{E}_a} = {}_1\hat{\mathbf{a}}(t) - {}_0\hat{\mathbf{a}}(t) - {}_0\hat{\mathbf{R}}(t) \cdot {}_0\hat{\alpha}(t)^\times \cdot {}_1\hat{\mathbf{p}} - {}_0\hat{\mathbf{R}}(t) \cdot [{}_0\hat{\omega}(t)^\times]^2 \cdot {}_1\hat{\mathbf{p}}, \quad (55)$$

The Jacobian of $r_{\mathcal{E}_R}$ over the states ${}_0\hat{\mathbf{R}}(t), {}_1\hat{\mathbf{R}}(t)$, and ${}_1\hat{\mathbf{R}}$ are found as:

$$\mathbf{J}_{{}_1\hat{\mathbf{R}}(t)}^{r_{\mathcal{E}_R}} = J_r^{-1}(r_{\mathcal{E}_R}), \quad (56)$$

$$\mathbf{J}_{{}_0\hat{\mathbf{R}}(t)}^{r_{\mathcal{E}_R}} = -J_r^{-1}(r_{\mathcal{E}_R}) \cdot {}_1\hat{\mathbf{R}}(t)^\top \cdot {}_0\hat{\mathbf{R}}(t), \quad (57)$$

$$\mathbf{J}_{{}_1\hat{\mathbf{R}}(t)}^{r_{\mathcal{E}_R}} = -J_r^{-1}(r_{\mathcal{E}_R}) \cdot {}_1\hat{\mathbf{R}}(t)^\top \cdot {}_0\hat{\mathbf{R}}(t) \cdot {}_1\hat{\mathbf{R}}, \quad (58)$$

Next, $r_{\mathcal{E}_R}$ will have the Jacobians with ${}_0\hat{\omega}(t), {}_1\hat{\omega}(t), {}_1\hat{\mathbf{R}}$:

$$\mathbf{J}_{{}_1\hat{\omega}(t)}^{r_{\mathcal{E}_\omega}} = {}_1\hat{\mathbf{R}}; \mathbf{J}_{{}_0\hat{\omega}(t)}^{r_{\mathcal{E}_\omega}} = -\mathbf{I}; \mathbf{J}_{{}_1\hat{\mathbf{R}}}^{r_{\mathcal{E}_\omega}} = -{}_1\hat{\mathbf{R}}_1\hat{\omega}(t)^\times. \quad (59)$$

Similarly, for $r_{\mathcal{E}_\alpha}$:

$$\mathbf{J}_{{}_1\hat{\alpha}(t)}^{r_{\mathcal{E}_\alpha}} = {}_1\hat{\mathbf{R}}; \mathbf{J}_{{}_0\hat{\alpha}(t)}^{r_{\mathcal{E}_\alpha}} = -\mathbf{I}; \mathbf{J}_{{}_1\hat{\mathbf{R}}}^{r_{\mathcal{E}_\alpha}} = -{}_1\hat{\mathbf{R}}_1\hat{\alpha}(t)^\times, \quad (60)$$

Next, $r_{\mathcal{E}_p}$ will have four non zero Jacobians:

$$\mathbf{J}_{{}_0\hat{\mathbf{R}}(t)}^{r_{\mathcal{E}_p}} = {}_0\hat{\mathbf{R}}(t) \cdot {}_1\hat{\mathbf{p}}(t)^\times, \quad (61)$$

$$\mathbf{J}_{{}_1\hat{\mathbf{p}}(t)}^{r_{\mathcal{E}_p}} = \mathbf{I}, \quad \mathbf{J}_{{}_0\hat{\mathbf{p}}(t)}^{r_{\mathcal{E}_p}} = -\mathbf{I}, \quad \mathbf{J}_{{}_1\hat{\mathbf{p}}}^{r_{\mathcal{E}_p}} = {}_0\hat{\mathbf{R}}(t). \quad (62)$$

For $r_{\mathcal{E}_v}$, we have:

$$\mathbf{J}_{{}_0\hat{\mathbf{R}}(t)}^{r_{\mathcal{E}_v}} = {}_0\hat{\mathbf{R}}(t) \cdot [{}_1\hat{\omega}(t)^\times \cdot {}_1\hat{\mathbf{p}}(t)]^\times, \quad (63)$$

$$\mathbf{J}_{{}_0\hat{\omega}(t)}^{r_{\mathcal{E}_v}} = {}_0\hat{\mathbf{R}}(t) \cdot {}_1\hat{\mathbf{p}}(t)^\times, \quad (64)$$

$$\mathbf{J}_{{}_1\hat{\mathbf{p}}(t)}^{r_{\mathcal{E}_v}} = -{}_0\hat{\mathbf{R}}(t) \cdot {}_0\hat{\omega}(t)^\times, \quad (65)$$

$$\mathbf{J}_{{}_1\hat{\mathbf{v}}(t)}^{r_{\mathcal{E}_v}} = \mathbf{I}, \quad \mathbf{J}_{{}_0\hat{\mathbf{v}}(t)}^{r_{\mathcal{E}_v}} = -\mathbf{I}. \quad (66)$$

Finally, the Jacobian of $r_{\mathcal{E}_a}$:

$$\begin{aligned} \mathbf{J}_{{}_0\hat{\mathbf{R}}(t)}^{r_{\mathcal{E}_a}} &= {}_0\hat{\mathbf{R}}(t) \cdot [{}_0\hat{\alpha}(t)^\times \cdot {}_1\hat{\mathbf{p}}(t)]^\times \\ &\quad + {}_0\hat{\mathbf{R}}(t) \cdot [{}_0\hat{\omega}(t)^\times]^2 \cdot {}_1\hat{\mathbf{p}}(t)^\times, \end{aligned} \quad (67)$$

$$\mathbf{J}_{{}_0\hat{\omega}(t)}^{r_{\mathcal{E}_a}} = -{}_0\hat{\mathbf{R}}(t) \cdot [{}_0\hat{\omega}(t)^\times {}_1\hat{\mathbf{p}}^\times - [{}_0\hat{\omega}(t)^\times \cdot {}_1\hat{\mathbf{p}}]^\times], \quad (68)$$

$$\mathbf{J}_{{}_0\hat{\alpha}(t)}^{r_{\mathcal{E}_a}} = {}_0\hat{\mathbf{R}}(t) \cdot {}_1\hat{\mathbf{p}}^\times \quad (69)$$

$$\mathbf{J}_{{}_1\hat{\mathbf{p}}(t)}^{r_{\mathcal{E}_a}} = -{}_0\hat{\mathbf{R}}(t) \cdot {}_0\hat{\alpha}(t)^\times - {}_0\hat{\mathbf{R}}(t) \cdot [{}_0\hat{\omega}(t)^\times]^2, \quad (70)$$

$$\mathbf{J}_{{}_1\hat{\mathbf{a}}(t)}^{r_{\mathcal{E}_a}} = \mathbf{I}, \quad \mathbf{J}_{{}_0\hat{\mathbf{a}}(t)}^{r_{\mathcal{E}_a}} = -\mathbf{I}. \quad (71)$$

7) *Marginalization prior*: In the context of sliding-window-based MAP optimization, *marginalization* is necessary to constrain the problem size without completely discarding past observation. The marginalization factor is constructed by first identifying the set of factors $\{r\}$ that will be removed when the window slides forward. Then we classify all state estimates coupled with $\{r\}$ into $\hat{\mathcal{X}}_\mu$ and $\hat{\mathcal{X}}_\kappa$, where $\hat{\mathcal{X}}_\mu$ are the states that will be marginalized (no longer updated), and $\hat{\mathcal{X}}_\kappa$ are those that will remain on the new sliding window. Hence, a marginalization factor coupled with $\hat{\mathcal{X}}_\kappa$ will be created using Schur Complement [29], which provides a prior value $\bar{\mathcal{X}}_\kappa$ and the information matrix $\mathbf{W}_{\mathcal{P}}$ as the weight of this factor.

IV. EXPERIMENT

A. Visual-Inertial Estimation and Calibration

We first validate the proposed CTME scheme on camera-IMU calibration using the same real-world dataset in [30], which was originally provided in [31]. A stereo-visual-inertial sensor suite is assembled and captures images at 20 Hz and inertial data at 200 Hz. A checkerboard is set up w.r.t. the world frame, and the ground-truth trajectory during calibration was recorded at about 100 Hz under aggressive motions using a motion capture system. We hereby demonstrate the double sphere camera model [32] used in this experiment

$$\pi(c_i \mathbf{l}) = \begin{bmatrix} f_x \frac{l_x}{d_3} + c_x \\ f_y \frac{l_y}{d_3} + c_y \end{bmatrix}, \quad \text{with} \quad (72)$$

$$d_3 = \beta d_2 + (1 - \beta)(\xi d_1 + l_z), \quad (73)$$

$$d_1 = \|\mathbf{l}\|, \quad \text{and} \quad d_2 = \sqrt{l_x^2 + l_y^2 + (\xi d_1 + l_z)^2}. \quad (74)$$

$c_i \mathbf{l} = [l_x, l_y, l_z]^\top$ denotes the landmark position represented w.r.t. camera frame, and $[f_x, f_y, c_x, c_y, \xi, \beta]^\top$ are the camera intrinsic parameters known from pre-calibration. We aim to calibrate the transformations $({}_{C_0}^I \mathbf{R}, {}_{C_0}^I \mathbf{p})$ and $({}_{C_1}^I \mathbf{R}, {}_{C_1}^I \mathbf{p})$ between the IMU and the two cameras, the IMU biases \mathbf{b}_ω , \mathbf{b}_a , the gravity \mathbf{g} , and estimate the trajectory of the IMU body frame at the same time. We set up the proposed method

TABLE I
COMPARISON OF CALIBRATION PARAMETERS ESTIMATED FROM THE PROPOSED GPTR AND THE SPLINE-BASED METHOD IN THE VISUAL-INERTIAL CALIBRATION, AND THE L_2 NORM OF THE DIFFERENCES.

State	GPTR (proposed)	B-Spline	Difference
${}^I_{C_0}\mathbf{R}$	$\begin{bmatrix} -0.99952700 & 0.00749704 & -0.0298349 \\ 0.02955570 & -0.03494170 & -0.9989520 \\ -0.00853167 & -0.99936100 & 0.0347036 \end{bmatrix}$	$\begin{bmatrix} -0.99952500 & 0.00760774 & -0.0298689 \\ 0.02958580 & -0.0349496 & -0.9989510 \\ -0.00864366 & -0.9993600 & 0.0347079 \end{bmatrix}$	1.5×10^{-4}
${}^I_{C_1}\mathbf{R}$	$\begin{bmatrix} -0.99952200 & 0.00808536 & -0.02984760 \\ 0.0299496 & 0.01280400 & -0.9994690 \\ -0.0076989 & -0.9998850 & -0.0130400 \end{bmatrix}$	$\begin{bmatrix} -0.99952 & 0.00819665 & -0.0298792 \\ 0.0299826 & 0.0127968 & -0.999469 \\ -0.00780993 & -0.999885 & -0.0130364 \end{bmatrix}$	1.2×10^{-4}
${}^I_{C_0}\mathbf{p}$	$(0.04542, -0.07189, -0.04637)$	$(0.04548, -0.07142, -0.04634)$	5.6×10^{-4}
${}^I_{C_1}\mathbf{p}$	$(-0.05553, -0.07044, -0.04913)$	$(-0.05546, -0.06997, -0.04911)$	5.6×10^{-4}
\mathbf{b}_ω	$10^{-5} \times (-2.95, 0.251, -1.94)$	$10^{-5} \times (-7.53, 0.224, -2.14)$	4.8×10^{-5}
\mathbf{b}_a	$10^{-3} \times (-0.67, -3.12, 0.38)$	$10^{-3} \times (-1.24, -7.33, 0.30)$	4.9×10^{-3}
\mathbf{g}	$(-0.03464, 9.6704, 1.44816)$	$(-0.03638, 9.67018, 1.45217)$	0.002

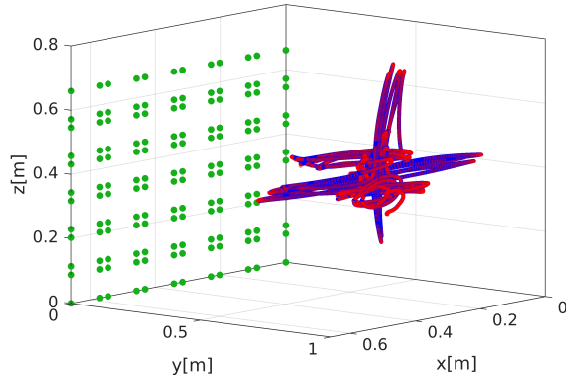


Fig. 3. Comparison of the estimated trajectory (blue) and ground truth (red) in the visual-inertial calibration given known landmark positions depicted as green dots.

using control points at 100 Hz for visual-inertial calibration and motion estimation in comparison with the continuous-time approach in [30] using cumulative B-splines. The initial guesses of the two approaches are identical as given in [30]. Fig. 3 shows the trajectory estimate given by the proposed method w.r.t. the ground truth. The RMSE of the absolute position error (APE) is computed as

$$\text{RMSE} = \sqrt{\frac{1}{N} \sum_{k=1}^N (\mathbf{p}_k - \hat{\mathbf{p}}_k)^2}, \quad (75)$$

where \mathbf{p}_k and $\hat{\mathbf{p}}_k$ are the ground truth and position estimates after alignment. The proposed approach delivers a RMSE of 7.7×10^{-4} m, which resembles the accuracy of the spline fitting method in [30] (with a RMSE of 8×10^{-4} m). The calibration results of the two approaches are listed in Tab. I. In general, the proposed approach shows comparable performance to the other continuous-time in [30] using B-splines.

B. Ultra-Wideband-Inertial Motion Estimation

We now evaluate the proposed method for 6-DoF motion estimation based on UWB-inertial sensor fusion. For this,

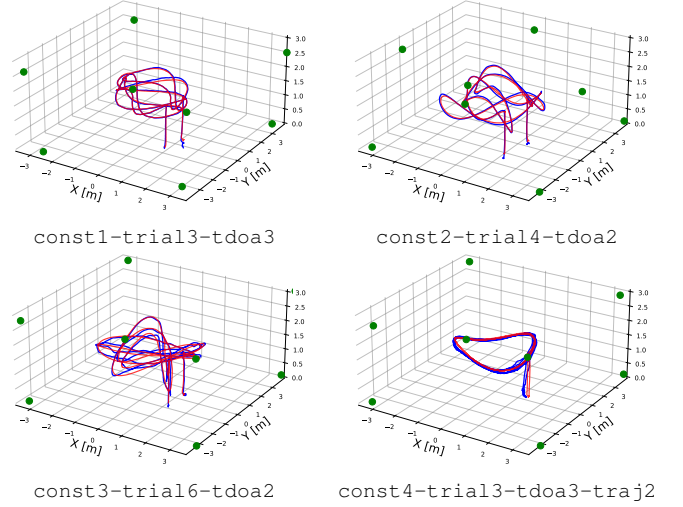


Fig. 4. Exemplary trajectories on UTIL dataset. Estimates in blue are compared to ground truth in red. Green dots are anchor positions.

we exploit the UTIL dataset [33] recorded onboard a moving quadcopter mounted with a 6-axis IMU and the UWB tag for time-difference-of-arrival (TDoA) ranging. Overall 79 sequences were recorded within UWB sensor networks of various anchor constellations (denoted by const1-4) and operation modes (centralized and decentralized, denoted as tdoa2 and tdoa3, respectively). The sequences also differ in TDoA measurement rates (200-500 Hz) and trajectories of dynamic motions. A few challenging conditions exist in a coupled manner, such as the absence of IMU readings, time-varying NLOS, complex interference induced by multiple static/dynamic obstacles of different types of materials (incl. ferromagnetic material), and multiple-path effect. For evaluation, we exploit the proposed method configured with the same set of parameters over all sequences and compare it with the error-state Kalman filter (ESKF) given by the dataset as baseline [33]. For the proposed method, motion estimates are delivered at the ground truth's time instant (at 200Hz) via GP interpolation, based on which we compute the RMSE of the APEs over the trajectory [34]. Four exemplary trajectories

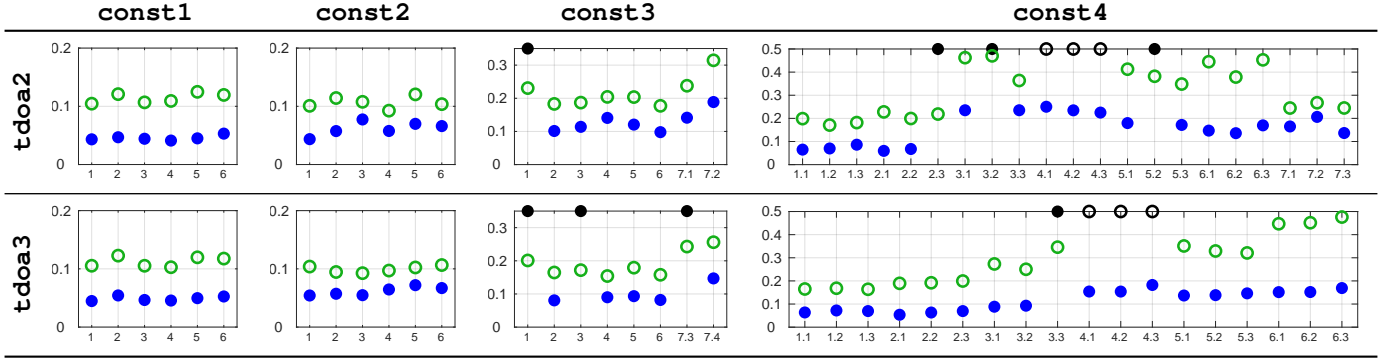


Fig. 5. APEs (RMSE) in meters (vertical axes) on all sequences of UTIL dataset. On the horizontal axes, we denote sequences according to `trial#`. In certain sequences, the index after dot denotes either `manual#` or `traj#`. This is straightforward to identify, given the original dataset. Results from GPTR and ESKF are plotted with \bullet and \circ , with tracking failures depicted as \bullet and \circ , respectively.

are shown in Fig. 4 for demonstration.

Shown in Fig. 5, the proposed method performs effectively on the whole dataset with failures only on very few sequences due to the harsh conditions and untuned parameters. In comparison with the baseline approach, it also delivers considerably better estimation accuracy with more than 50% of improvement in certain challenging scenarios.

C. Multi-LiDAR Coupled Odometry

In this section we first conduct an experiment of the MLCME scheme on a handheld setup with two lidars. Next, we present a new experiment on synthetic data sequence, where we can have perfect ground truth, and showcase an online extrinsic estimation scenario. Finally, we conduct another experiment on the MCD dataset [35], to demonstrate the capability of the GPTR scheme to track aggressive motions. Two state-of-the-art lidar-only lidar-odometry (LO) methods are selected for comparison, namely I2EKF-LO [36] and Traj-LO [37]. In the frontend, both of these methods are direct methods, i.e. the lidar points are directly associated with the map to build the point-to-plane factor (46) without feature extraction. In the backend, we also disable the mapping process and only use a fixed prior map for all methods. The similarities in both frontend and backend allow us to focus the comparison on the trajectory representation only. Specifically, I2EKF uses a discrete-time representation, with the second-order kinematic model (random acceleration) for both rotation and translation states. On the other hand, Traj-LO uses CT GP-based representation, with second-order kinematic model for the rotation states, and third-order kinematics for the translation states.

1) *Real world handheld setup*: We first test the multi-lidar calibration scheme on a real-world setup as shown in Fig. 6, which consists of two Livox-Mid360 lidars. We use the datasheet illustration, as well as the hardware CAD model to deduce the ground truth for the extrinsics. The trajectory ground truth is obtained from a motion capture system, with careful compensation for the reflective markers and the lidar's frame of reference.

Figure 7 shows the trajectory estimates of the lidars and the ground truth. It can be seen that in this experiment the

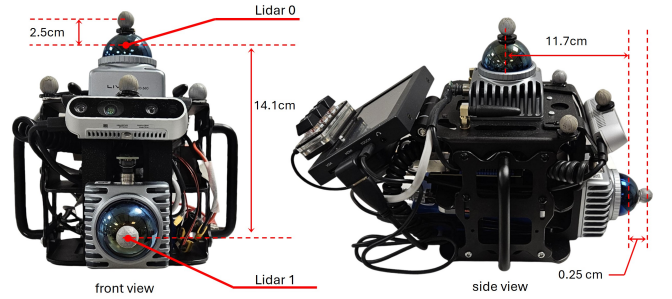


Fig. 6. The two-lidar sensor suite. Based on the illustration in the Mid360 Datasheet, we assume the origin of the lidar's coordinate system coincides with the center of the half-spheres.

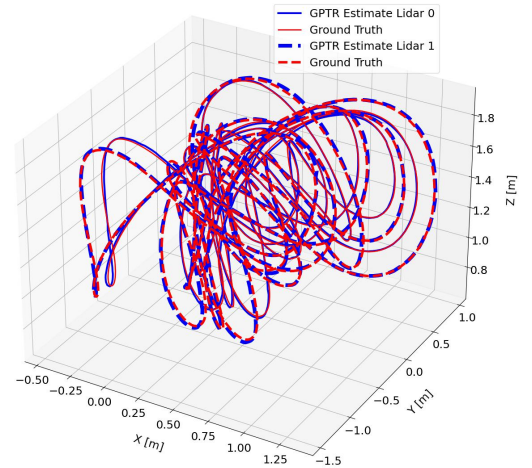


Fig. 7. Trajectory estimate for each lidar by the MLCME scheme vs the ground truth.

motion is quite aggressive, where the setup is swung around in the experiment area. We calculate the APE of the trajectory estimates from I2EKF, Traj-LO and our method, and report it in Tab. II. The table shows that the MLCME scheme receives the highest accuracy. In this experiment, I2EKF diverges due to aggressive motion. In Fig. 9, we can also see that the extrinsic parameters converge to some constant values which is within

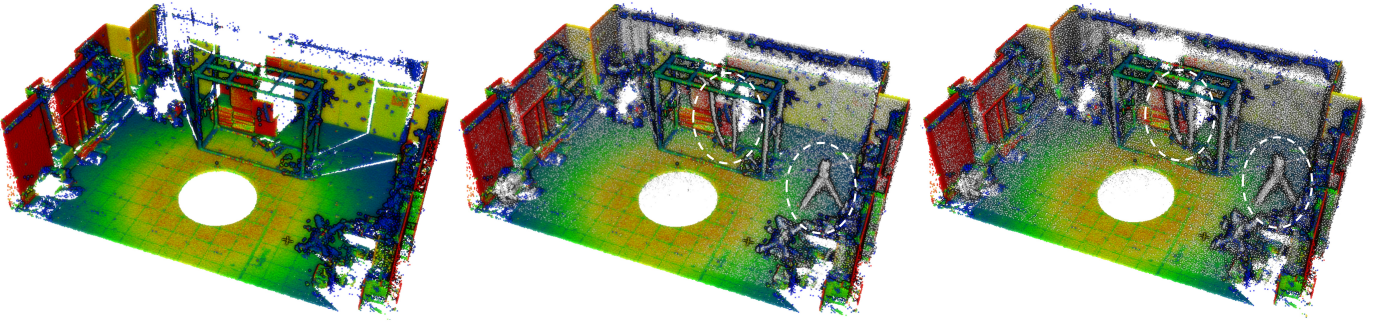


Fig. 8. Left: the prior map. Middle: the lidar pointclouds undistorted and overlaid on the prior map. Right: the distorted raw pointcloud over the prior map.

TABLE II
COMPARING THE APE OF TRAJECTORY ESTIMATE BY GPTR
MLCME SCHEME AND OTHER METHODS WITH THE
HANDHELD SETUP DATA.

Lidar	I2EKF-LO	Traj-LO	GPTR-U	GPTR-C
0	x	0.02804	0.02366	0.023344
1	x	0.03006	0.02117	0.02046

Note: All values are in [m] unit. **GPTR-C** refers to the result from the MLCME scheme, while **GPTR-U** refers to CTME on separate lidars without coupling.

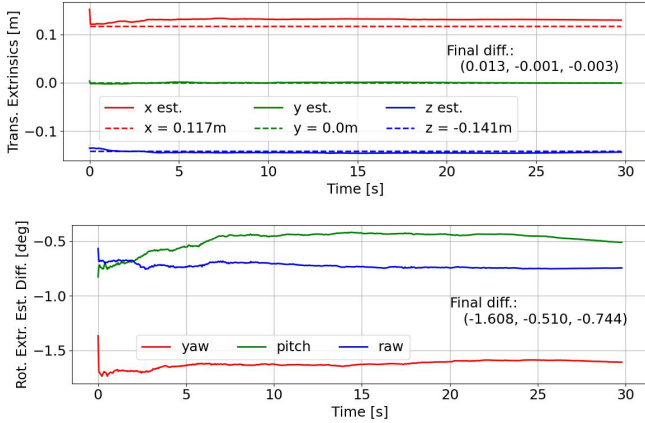


Fig. 9. The extrinsic estimate result between LiDAR 0 and LiDAR 1.

1.5cm and 2° from our assumed ground truth. In Fig. 8, we also show the pointclouds undistorted by the CT trajectory overlaid on top of the prior map, compared to that without distortion.

2) *Synthetic data:* In generating the synthetic dataset, we assume two LiDARs, 0 and 1, are mounted on a vehicle (see Fig. 10) and their extrinsics are set as a user-defined parameter. The trajectory of the vehicle is predetermined by a continuous function over a 30s time period. We then sample the vehicle's pose every 0.02 ms, convert it to the LiDAR's pose, perform ray-tracing to the walls of a $6\text{m} \times 6\text{m}$ room to obtain the distance, add a Gaussian noise of 0.02m variance to the range, and finally calculate the 3D point. The coordinate of LiDAR 0 and LiDAR 1 in the robot body frame expressed in a yaw-

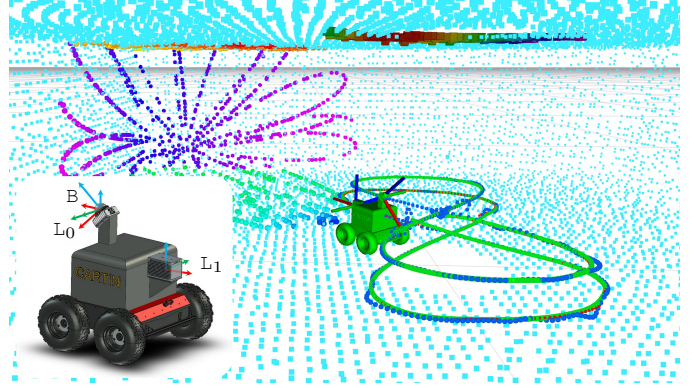


Fig. 10. Simulated setup with two LiDARs mounted on top of a ground robot. The ground robot moves in a room with six flat sides. The two LiDARs have no overlap. The GPTR trajectory and I2EKF-LO estimates are marked by green and blue respectively, while the ground truth trajectories are in red.

pitch-roll-x-y-z tuple is set as:

$$\begin{aligned} {}^{B}_{L_0} \mathbf{T} &= (45^\circ, 0, 0, 0, 0, 0) \\ {}^{B}_{L_1} \mathbf{T} &= \begin{cases} (180^\circ, 0, 0, -0.5, 0, -0.25), & \text{if } t \notin (10, 20) \\ (180^\circ, 0, 0, -0.5, 0, -0.35), & \text{otherwise.} \end{cases} \end{aligned}$$

Hence, the two LiDARs' FOV do not overlap. From ${}^{B}_{L_0} \mathbf{T}$ and ${}^{B}_{L_1} \mathbf{T}$ we can calculate the transform between L_0 and L_1 as

$$\begin{aligned} {}^{L_0}_{L_1} \mathbf{T} &= (180^\circ, 45^\circ, 0, \frac{-1}{4\sqrt{2}}, 0, \frac{-3}{4\sqrt{2}}) \\ &\approx (180^\circ, 45^\circ, 0, -0.177, -0.530), \text{ if } t \notin (10, 20) \end{aligned}$$

and

$$\begin{aligned} {}^{L_0}_{L_1} \mathbf{T} &= (180^\circ, 45^\circ, 0, \frac{-3}{20\sqrt{2}}, 0, \frac{-17}{20\sqrt{2}}) \\ &\approx (180^\circ, 45^\circ, 0, -0.106, -0.601), \text{ if } t \in (10, 20), \end{aligned}$$

which is the ground truth for the MLCME scheme. The change of extrinsic mimics a scenario where the sensor mechanical holder may slip during operation. The LiDAR initial poses are set with 10cm translation and 5° rotation errors. The knot length is chosen to be 0.02204s.

From Fig. 10, Fig. 11, we can see that the MLCME scheme can estimate the LiDAR extrinsic with high accuracy. The extrinsic parameters converge quickly within the first few seconds, and at $t = 10$ when there is a significant change in the extrinsic parameters, the MLCME scheme can quickly

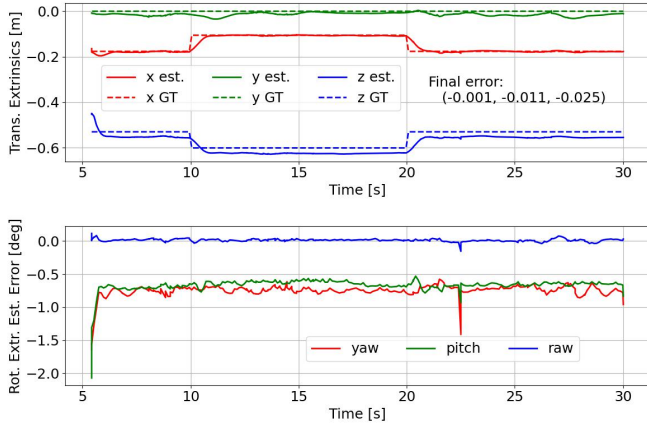


Fig. 11. The estimation error of the extrinsic parameters between LiDAR 0 and LiDAR 1.

TABLE III
COMPARING THE APE OF TRAJECTORY ESTIMATE BY GPTR
MLCME SCHEME AND OTHER METHODS WITH THE
SYNTHETIC DATA.

Lidar	I2EKF-LO	Traj-LO	GPTR-U	GPTR-C
0	0.06964	0.04285	0.01981	0.01975
1	0.04608	0.04138	0.02497	0.02353

Note: All values are in [m] unit. **GPTR-C** refers to the result from the MLCME scheme, while **GPTR-U** refers to CTME on separate lidars without coupling.

correct its estimate. Table III also shows that our approach achieves the lowest APE.

Remark 4. Our example above demonstrates the efficacy of GPTR in a multi-trajectory calibration scenario, thus a map of the room was assumed available (in practice it can be obtained by using a 3D scanner, or by stitching together some static LiDAR scans). Without a prior map, one can adopt a batch optimization scheme with iterative feature matching [38]–[40]. The example can also be modified to become a full-fledged LOAM system with online calibration by integrating some incremental mapping technique, for e.g. ikd-Tree [41], VoxelMap [42], UFOMap [43]. To the best of our knowledge, few works have addressed the online calibration of multi-LiDAR systems, and most works often assume a constant LiDAR extrinsic. In the rare case of M-LIOM [44] that does consider online calibration, the method requires overlap between sensors for it to work.

3) *MCD dataset*: In the synthetic dataset, the maximum velocity is about 0.5m/s and the handheld setup about 3m/s. To stress-test the estimation schemes, we select one sequence of MCD [35] that was recorded on a high-speed All-Terrain-Vehicle (ATV) which features high-speed motion (the translational velocity can be up to 10m/s, and angular velocity up to 1 rad/s). As shown in Fig. 12, only our approach can maintain tracking against the aggressive motion, whereas the other methods will lose track at hard turns, causing the estimate to diverge. This demonstrates the capability of our trajectory representation against those of I2EKF and Traj-LO.

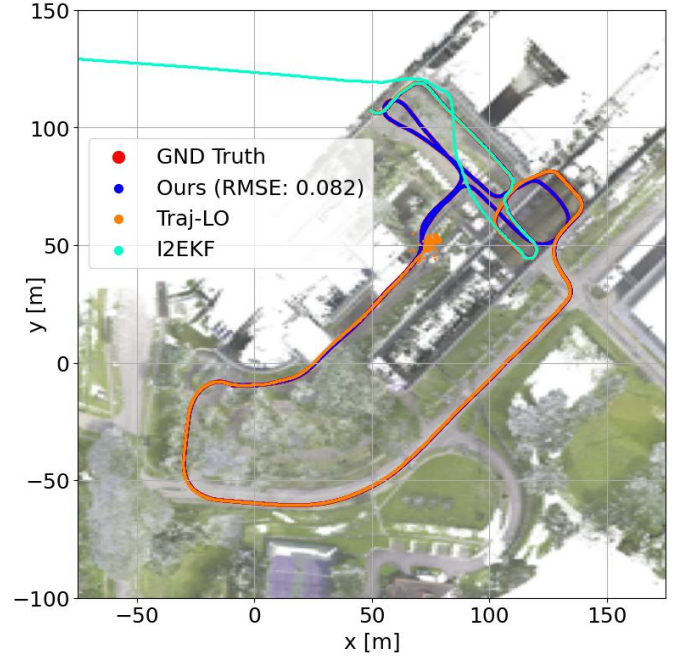


Fig. 12. The trajectory estimate of one lidar by different methods in MCD sequence ntu_day_01.

Remark 5. We only show the result of one sequence of MCD as the result is the same with other five ATV sequences (the ntu_* sequences). We also note that to make the code illustrative and easier for readers to modify, we have used a ceres-based implementation to solve the problem (30). In [16], such an implementation was shown to be inefficient, and a more efficient approach can be adopted by using a custom solver based on the Eigen library as in SLICT2 or Traj-LO.

V. CONCLUSION AND FUTURE WORKS

In this paper, we have developed a CTME framework based on the Gaussian Process named GPTR. The framework features a third-order trajectory representation for both rotational and translational states. To facilitate easy adoption of GPTR, the source code is developed as a header-only library that can be imported to any project. Moreover, it provides a comprehensive set of working examples of motion estimation based on GPTR, leveraging LiDAR, visual, IMU, and UWB factors in both batch-optimization and sliding-window optimization schemes. Based on our examples, we hope the community can come up with more advanced motion estimation schemes featuring other sensing models. The source code of GPTR has been open-sourced at <https://github.com/brytsknguyen/gptr> and we welcome all feedback and contributions from the community to improve our project.

APPENDIX A

CLOSED FORMS OF $J_r(\theta)$, $J_r^{-1}(\theta)$, $H_\theta(\theta, \dot{\theta})$ AND $H'_\theta(\theta, \omega)$

We recall the closed forms of J_r and J_r^{-1} as provided in [45]. Based on these formulas, we apply the chain rule and product rules on terms of J_r and J_r^{-1} to arrive at the closed

forms of $H_\theta(\theta, \dot{\theta})$ and $H'_\theta(\theta, \omega)$. Specifically,

$$\begin{aligned} J_r(\theta) &= I - g(\vartheta)\theta^\times + h(\vartheta)(\theta^\times)^2; \\ J_r^{-1}(\theta) &= I + \frac{1}{2}\theta^\times + g'(\vartheta)(\theta^\times)^2; \\ H_\theta(\theta, \dot{\theta}) &= \dot{\theta}^\times g(\vartheta) + \dot{\theta}^\times \theta g_\vartheta(\vartheta) \bar{\theta}^\top + f_u(\theta, \dot{\theta})h(\vartheta) \dots \\ &\quad \dots + f(\theta, \dot{\theta})h_\vartheta(\vartheta) \bar{\theta}^\top; \\ H'_\theta(\theta, \omega) &= -\frac{1}{2}\omega^\times + f_u(\theta, \omega)g'(\vartheta) + f(\theta, \omega)g'_\vartheta(\vartheta) \bar{\theta}^\top; \end{aligned}$$

with the intermediaries defined as follows:

$$\vartheta \triangleq \|\theta\|, \quad \bar{\theta} \triangleq \frac{\theta}{\vartheta}, \quad \bar{\theta}_\theta = \frac{\partial \bar{\theta}}{\partial \theta} \triangleq (I - \bar{\theta} \bar{\theta}^\top) \frac{1}{\vartheta}; \quad (76)$$

$$f(u, v) \triangleq (u^\times)^2 v, \quad f_v(u, v) \triangleq (u^\times)^2, \quad (77)$$

$$f_u(u, v) \triangleq -u^\times v^\times - (u^\times v)^\times, \quad (78)$$

$$f_{uu}(u, v, w) \triangleq (v^\times w)^\times - w^\times v^\times, \quad (79)$$

$$f_{uv}(u, v, w) \triangleq u^\times w^\times + w^\times u^\times, \quad (80)$$

$$g(\vartheta) \triangleq \frac{1 - \cos \vartheta}{\vartheta^2}, \quad (81)$$

$$g_\vartheta(\vartheta) = \frac{\partial g(\vartheta)}{\partial \vartheta} = \frac{\sin \vartheta}{\vartheta^2} + \frac{2(\cos \vartheta - 1)}{\vartheta^3}, \quad (82)$$

$$\begin{aligned} g_{\vartheta\vartheta}(\vartheta) &= \frac{\partial^2 g(\vartheta)}{\partial \vartheta^2} = \frac{\cos \vartheta}{\vartheta^2} - \frac{4 \sin \vartheta}{\vartheta^3} \\ &\quad + \frac{6(1 - \cos \vartheta)}{\vartheta^4}; \end{aligned} \quad (83)$$

$$h(\vartheta) \triangleq \frac{\vartheta - \sin \vartheta}{\vartheta^3}, \quad (84)$$

$$h_\vartheta(\vartheta) = \frac{\partial h(\vartheta)}{\partial \vartheta} = -\frac{2}{\vartheta^3} - \frac{\cos \vartheta}{\vartheta^3} + \frac{3 \sin \vartheta}{\vartheta^4}, \quad (85)$$

$$\begin{aligned} h_{\vartheta\vartheta}(\vartheta) &= \frac{\partial^2 h(\vartheta)}{\partial \vartheta^2} = \frac{\sin \vartheta}{\vartheta^3} + \frac{6(\cos \vartheta + 1)}{\vartheta^4} \\ &\quad - \frac{12 \sin \vartheta}{\vartheta^5}; \end{aligned} \quad (86)$$

$$g'(\vartheta) \triangleq \frac{1}{\vartheta^2} - \frac{1 + \cos \vartheta}{2\vartheta \sin \vartheta}, \quad (87)$$

$$g'_\vartheta(\vartheta) = \frac{\partial g'(\vartheta)}{\partial \vartheta} = \frac{-2}{\vartheta^3} + \frac{(1 + \cos \vartheta)(\vartheta + \sin \vartheta)}{2\vartheta^2(\sin \vartheta)^2}, \quad (88)$$

$$\begin{aligned} g'_{\vartheta\vartheta}(\vartheta) &= \frac{\partial^2 g'(\vartheta)}{\partial \vartheta^2} = \frac{6}{\vartheta^4} + \frac{\sin \vartheta}{\vartheta^3(\cos \vartheta - 1)} \\ &\quad + \frac{\vartheta \cos \vartheta + 2 \sin \vartheta + \vartheta}{2\vartheta^2 \sin \vartheta(\cos \vartheta - 1)}. \end{aligned} \quad (89)$$

With the definitions above, we also define the following that will be referenced in Appendix B:

$$\begin{aligned} L_{\theta\theta}(\theta, \dot{\theta}, \dot{\theta}) &= \frac{\partial H_\theta(\theta, \dot{\theta})}{\partial \theta} \\ &= \dot{\theta}^\times \dot{\theta} g_\vartheta(\vartheta) \bar{\theta}^\top \\ &\quad + \dot{\theta}^\times g_\vartheta(\vartheta)(\bar{\theta}^\top \dot{\theta}) + \dot{\theta}^\times \theta(\bar{\theta}^\top \dot{\theta})g_{\vartheta\vartheta}(\vartheta) \bar{\theta}^\top \\ &\quad + \dot{\theta}^\times \theta g_\vartheta(\vartheta) \dot{\theta}^\top \bar{\theta}_\theta \\ &\quad + f_{uu}(\theta, \dot{\theta}, \dot{\theta})h(\vartheta) + f_u(\theta, \dot{\theta})\dot{\theta} h_\vartheta(\vartheta) \bar{\theta}^\top \\ &\quad + f_u(\theta, \dot{\theta})(\bar{\theta}^\top \dot{\theta})h_\vartheta(\vartheta) + f(\theta, \dot{\theta})h_\vartheta(\vartheta) \dot{\theta}^\top \bar{\theta}_\theta \\ &\quad + f(\theta, \dot{\theta})(\bar{\theta}^\top \dot{\theta})h_{\vartheta\vartheta}(\vartheta) \bar{\theta}^\top, \end{aligned} \quad (90)$$

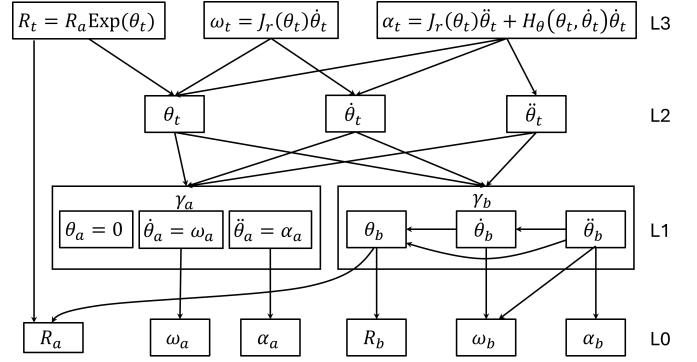


Fig. 13. The hierarchy of manifold variables: We group them into four levels, and the goal is to find the Jacobian of variables in level L3 w.r.t to variables in level L0. Every arrow from variable v_i to v_j represents a non-zero partial derivative $J_{v_j}^{v_i}$. To avoid clustering, every arrow that goes into the sub-group γ_a or γ_b represent three actual arrows, each pointing to each variable in the subgroup.

$$\begin{aligned} L_{\theta\theta}(\theta, \dot{\theta}, \dot{\theta}) &= \frac{\partial H_\theta(\theta, \dot{\theta})}{\partial \dot{\theta}} w \Big|_{w=\dot{\theta}} \\ &= -\dot{\theta}^\times g(\vartheta) - \theta g_\vartheta(\vartheta) \bar{\theta}^\top \dot{\theta} + f_{uv}(\theta, \dot{\theta}, \dot{\theta})h(\vartheta) \\ &\quad + f_v(\theta, \dot{\theta})h_\vartheta(\vartheta) \bar{\theta}^\top \dot{\theta}, \end{aligned} \quad (91)$$

$$\begin{aligned} L'_{\theta\theta}(\theta, \omega, \dot{\theta}) &= \frac{\partial H'_\theta(\theta, \omega)}{\partial \theta} \\ &= f_{uu}(\theta, \omega, \dot{\theta})g'(\vartheta) + f_u(\theta, \omega)\dot{\theta} g'_\vartheta(\vartheta) \bar{\theta}^\top \\ &\quad + f_u(\theta, \omega)(\bar{\theta}^\top \dot{\theta})g'_\vartheta(\vartheta) + f(\theta, \omega)g'_\vartheta(\vartheta) \dot{\theta}^\top \bar{\theta}_\theta \\ &\quad + f(\theta, \omega)(\bar{\theta}^\top \dot{\theta})g'_{\vartheta\vartheta}(\vartheta) \bar{\theta}^\top, \end{aligned} \quad (92)$$

$$\begin{aligned} L'_{\theta\omega}(\theta, \omega, \dot{\theta}) &= \frac{\partial H'_\theta(\theta, \omega)}{\partial \omega} \\ &= \frac{1}{2}\dot{\theta}^\times + f_{uv}(\theta, \omega, \dot{\theta})g'(\vartheta) + f_v(\theta, \omega)g'_\vartheta(\vartheta)(\bar{\theta}^\top \dot{\theta}). \end{aligned} \quad (93)$$

APPENDIX B CALCULATING THE JACOBIANS $\frac{\partial \mathcal{X}_t}{\partial \mathcal{X}_a}$ AND $\frac{\partial \mathcal{X}_t}{\partial \mathcal{X}_b}$

To simplify the notation, let us denote $\mathbf{J}_{\mathcal{X}}^{\mathcal{Y}} \triangleq \frac{\partial \mathcal{Y}}{\partial \mathcal{X}}$. In Fig. 13, we provide a diagram of the relationship between the variables. Our goal is to find all of the Jacobians $\mathbf{J}_{\mathcal{X}}^{\mathcal{Y}}$ where \mathcal{Y} belongs to L3 and \mathcal{X} belongs to L0. This can be done in a layer-by-layer manner as follows.

First, we calculate the Jacobians of variables in L1 over those in L0. By using the diagram in Fig. 13, we can identify eleven different paths from L1 to L0, each path can be represented by one Jacobian, specifically:

$$\mathbf{J}_{\omega_a}^{\theta_a} = I, \quad \mathbf{J}_{\alpha_a}^{\theta_a} = I, \quad (94)$$

$$\mathbf{J}_{\mathbf{R}_a}^{\theta_b} = \frac{\partial \text{Log}(\mathbf{R}_a^{-1} \mathbf{R}_b)}{\partial \mathbf{R}_a} = -J_r^{-1}(\theta_b)[\mathbf{R}_a^{-1} \mathbf{R}_b]^{-1}, \quad (95)$$

$$\mathbf{J}_{\mathbf{R}_b}^{\theta_b} = \frac{\partial \text{Log}(\mathbf{R}_a^{-1} \mathbf{R}_b)}{\partial \mathbf{R}_b} = J_r^{-1}(\theta_b), \quad (96)$$

$$\begin{aligned} \mathbf{J}_{\mathbf{R}_a}^{\dot{\theta}_b} &= \frac{\partial[J_r^{-1}(\theta_b)\omega_b]}{\partial \mathbf{R}_a} = \frac{\partial[J_r^{-1}(\theta_b)\omega_b]}{\partial \theta_b} \frac{\partial \theta_b}{\partial \mathbf{R}_a} \\ &= H'_{\theta_b}(\theta_b, \omega_b) \mathbf{J}_{\mathbf{R}_a}^{\theta_b}, \end{aligned} \quad (97)$$

$$\mathbf{J}_{\mathbf{R}_b}^{\dot{\theta}_b} = \frac{\partial[J_r^{-1}(\theta_b)\omega_b]}{\partial \mathbf{R}_b} = H'_{\theta_b}(\theta_b, \omega_b) \mathbf{J}_{\mathbf{R}_b}^{\theta_b}, \quad (98)$$

$$\mathbf{J}_{\omega_b}^{\dot{\theta}_b} = J_r^{-1}(\theta_b), \quad (99)$$

$$\begin{aligned} \mathbf{J}_{\mathbf{R}_a}^{\ddot{\theta}_b} &= \frac{\partial[J_r^{-1}(\theta_b)\alpha_b + H'_{\theta_b}(\theta_b, \omega_b)\dot{\theta}_b]}{\partial \mathbf{R}_a} \\ &= H'_{\theta_b}(\theta_b, \alpha_b) \mathbf{J}_{\mathbf{R}_a}^{\theta_b} + H'_{\theta_b}(\theta_b, \omega_b) \mathbf{J}_{\mathbf{R}_a}^{\dot{\theta}_b} \\ &\quad + L'_{\theta_b\theta_b}(\theta_b, \omega_b, \dot{\theta}_b) \mathbf{J}_{\mathbf{R}_a}^{\theta_b} \end{aligned} \quad (100)$$

$$\begin{aligned} \mathbf{J}_{\mathbf{R}_b}^{\ddot{\theta}_b} &= H'_{\theta_b}(\theta_b, \alpha_b) \mathbf{J}_{\mathbf{R}_b}^{\theta_b} + H'_{\theta_b}(\theta_b, \omega_b) \mathbf{J}_{\mathbf{R}_b}^{\dot{\theta}_b} \\ &\quad + L'_{\theta_b\theta_b}(\theta_b, \omega_b, \dot{\theta}_b) \mathbf{J}_{\mathbf{R}_b}^{\theta_b} \end{aligned} \quad (101)$$

$$\mathbf{J}_{\omega_b}^{\ddot{\theta}_b} = L'_{\theta_b\omega_b}(\theta_b, \omega_b, \dot{\theta}_b) + H'_{\theta_b}(\theta_b, \omega_b) \mathbf{J}_{\omega_b}^{\dot{\theta}_b} \quad (102)$$

$$\mathbf{J}_{\alpha_b}^{\ddot{\theta}_b} = J_r^{-1}(\theta_b) \quad (103)$$

Next for the Jacobians between L2 and L1, from (4) we have the following interpolation relationship:

$$\begin{bmatrix} \theta_t \\ \dot{\theta}_t \\ \ddot{\theta}_t \end{bmatrix} = \begin{bmatrix} \Lambda_{00} & \Lambda_{01} & \Lambda_{02} \\ \Lambda_{10} & \Lambda_{11} & \Lambda_{12} \\ \Lambda_{20} & \Lambda_{21} & \Lambda_{22} \end{bmatrix} \begin{bmatrix} \theta_a \\ \dot{\theta}_a \\ \ddot{\theta}_a \end{bmatrix} \quad (104)$$

$$+ \begin{bmatrix} \Psi_{00} & \Psi_{01} & \Psi_{02} \\ \Psi_{10} & \Psi_{11} & \Psi_{12} \\ \Psi_{20} & \Psi_{21} & \Psi_{22} \end{bmatrix} \begin{bmatrix} \theta_b \\ \dot{\theta}_b \\ \ddot{\theta}_b \end{bmatrix} \quad (105)$$

where $\Lambda_{ij}, \Psi_{ij} \in \mathbb{R}^{3 \times 3}$ are some 3×3 blocks of $\Lambda(\tau)$ and $\Psi(\tau)$. Thus, the Jacobians from L2 to L1 can be easily calculated as:

$$\mathbf{J}_{\theta_a}^{\theta_t(i)} = \Lambda_{i,j}, \quad \mathbf{J}_{\theta_b}^{\theta_t(i)} = \Psi_{i,j}, \quad i, j \in 0, 1, 2, \quad (106)$$

where $\theta^{(0)} \triangleq \theta$, $\theta^{(1)} \triangleq \dot{\theta}$, and $\theta^{(2)} \triangleq \ddot{\theta}$.

Finally for the Jacobian from L3 to L2, from the mappings (20), we have:

$$\mathbf{J}_{\theta_t}^{\mathbf{R}_t} = \frac{\partial \mathbf{R}_a \text{Exp}(\theta_t)}{\partial \theta_t} = J_r(\theta_t), \quad (107)$$

$$\mathbf{J}_{\theta_t}^{\omega_t} = \frac{\partial J_r(\theta_t)\dot{\theta}_t}{\partial \theta_t} = H_{\theta_t}(\theta_t, \dot{\theta}_t), \quad (108)$$

$$\mathbf{J}_{\theta_t}^{\omega_t} = \frac{\partial J_r(\theta_t)\dot{\theta}_t}{\partial \dot{\theta}_t} = J_r(\theta_t), \quad (109)$$

$$\mathbf{J}_{\theta_t}^{\alpha_t} = H_{\theta_t}(\theta_t, \ddot{\theta}_t) + L_{\theta_t\theta_t}(\theta_t, \dot{\theta}_t, \ddot{\theta}_t), \quad (110)$$

$$\mathbf{J}_{\dot{\theta}_t}^{\alpha_t} = L_{\theta_t\dot{\theta}_t}(\theta_t, \dot{\theta}_t, \ddot{\theta}_t) + H_{\theta_t}(\theta_t, \ddot{\theta}_t), \quad (111)$$

$$\mathbf{J}_{\ddot{\theta}_t}^{\alpha_t} = J_r(\theta_t). \quad (112)$$

Now, let us compute the following Jacobians from L2 to L0, using the L2-L1 and L1-L0 Jacobians:

$$\mathbf{J}_{\mathbf{R}_a}^{\theta_t(i)} = \mathbf{J}_{\theta_b}^{\theta_t(i)} \mathbf{J}_{\mathbf{R}_a}^{\theta_b} + \mathbf{J}_{\dot{\theta}_b}^{\theta_t(i)} \mathbf{J}_{\mathbf{R}_a}^{\dot{\theta}_b} + \mathbf{J}_{\ddot{\theta}_b}^{\theta_t(i)} \mathbf{J}_{\mathbf{R}_a}^{\ddot{\theta}_b}, \quad (113)$$

$$\mathbf{J}_{\mathbf{R}_b}^{\theta_t(i)} = \mathbf{J}_{\theta_b}^{\theta_t(i)} \mathbf{J}_{\mathbf{R}_b}^{\theta_b} + \mathbf{J}_{\dot{\theta}_b}^{\theta_t(i)} \mathbf{J}_{\mathbf{R}_b}^{\dot{\theta}_b} + \mathbf{J}_{\ddot{\theta}_b}^{\theta_t(i)} \mathbf{J}_{\mathbf{R}_b}^{\ddot{\theta}_b}, \quad (114)$$

$$\mathbf{J}_{\omega_a}^{\theta_t(i)} = \mathbf{J}_{\theta_a}^{\theta_t(i)} \mathbf{J}_{\omega_a}^{\theta_a}, \quad \mathbf{J}_{\omega_b}^{\theta_t(i)} = \mathbf{J}_{\theta_b}^{\theta_t(i)} \mathbf{J}_{\omega_b}^{\theta_b} + \mathbf{J}_{\dot{\theta}_b}^{\theta_t(i)} \mathbf{J}_{\omega_b}^{\dot{\theta}_b}, \quad (115)$$

$$\mathbf{J}_{\alpha_a}^{\theta_t(i)} = \mathbf{J}_{\theta_a}^{\theta_t(i)} \mathbf{J}_{\alpha_a}^{\theta_a}, \quad \mathbf{J}_{\alpha_b}^{\theta_t(i)} = \mathbf{J}_{\theta_b}^{\theta_t(i)} \mathbf{J}_{\alpha_b}^{\theta_b}, \quad i \in \{0, 1, 2\}. \quad (116)$$

Moving on to L3, we note that there is one direct connection from L3 to L0, which corresponds to the partial derivative:

$$\frac{\partial \mathbf{R}_a \text{Exp}(\phi)}{\partial \mathbf{R}_a} \Big|_{\phi=\theta_t} = \text{Exp}(\theta_t)^{-1} = \text{Exp}(-\theta_t). \quad (117)$$

Finally, we can find the L3-L0 Jacobians from (117) and the L3-L2 and L2-L0 Jacobians above. For \mathbf{R}_t , we have:

$$\mathbf{J}_{\mathbf{R}_a}^{\mathbf{R}_t} = \text{Exp}(-\theta_t) + \mathbf{J}_{\theta_t}^{\mathbf{R}_t} \mathbf{J}_{\mathbf{R}_a}^{\theta_t}, \quad \mathbf{J}_{\mathbf{R}_b}^{\mathbf{R}_t} = \mathbf{J}_{\theta_t}^{\mathbf{R}_t} \mathbf{J}_{\mathbf{R}_b}^{\theta_t}, \quad (118)$$

$$\mathbf{J}_{\omega_a}^{\mathbf{R}_t} = \mathbf{J}_{\theta_t}^{\mathbf{R}_t} \mathbf{J}_{\omega_a}^{\theta_t}, \quad \mathbf{J}_{\omega_b}^{\mathbf{R}_t} = \mathbf{J}_{\theta_t}^{\mathbf{R}_t} \mathbf{J}_{\omega_b}^{\theta_t}, \quad (119)$$

$$\mathbf{J}_{\alpha_a}^{\mathbf{R}_t} = \mathbf{J}_{\theta_t}^{\mathbf{R}_t} \mathbf{J}_{\alpha_a}^{\theta_t}, \quad \mathbf{J}_{\alpha_b}^{\mathbf{R}_t} = \mathbf{J}_{\theta_t}^{\mathbf{R}_t} \mathbf{J}_{\alpha_b}^{\theta_t}, \quad (120)$$

and similarly, for ω_t and α_t :

$$\mathbf{J}_{\mathbf{R}_j}^{\omega_t} = \mathbf{J}_{\theta_t}^{\omega_t} \mathbf{J}_{\mathbf{R}_j}^{\theta_t} + \mathbf{J}_{\dot{\theta}_t}^{\omega_t} \mathbf{J}_{\mathbf{R}_j}^{\dot{\theta}_t}, \quad (121)$$

$$\mathbf{J}_{\omega_j}^{\omega_t} = \mathbf{J}_{\theta_t}^{\omega_t} \mathbf{J}_{\omega_j}^{\theta_t} + \mathbf{J}_{\dot{\theta}_t}^{\omega_t} \mathbf{J}_{\omega_j}^{\dot{\theta}_t}, \quad (122)$$

$$\mathbf{J}_{\alpha_j}^{\omega_t} = \mathbf{J}_{\theta_t}^{\omega_t} \mathbf{J}_{\alpha_j}^{\theta_t} + \mathbf{J}_{\dot{\theta}_t}^{\omega_t} \mathbf{J}_{\alpha_j}^{\dot{\theta}_t}, \quad (123)$$

$$\mathbf{J}_{\mathbf{R}_i}^{\alpha_t} = \mathbf{J}_{\theta_t}^{\alpha_t} \mathbf{J}_{\mathbf{R}_i}^{\theta_t} + \mathbf{J}_{\dot{\theta}_t}^{\alpha_t} \mathbf{J}_{\mathbf{R}_i}^{\dot{\theta}_t} + \mathbf{J}_{\ddot{\theta}_t}^{\alpha_t} \mathbf{J}_{\mathbf{R}_i}^{\ddot{\theta}_t}, \quad (124)$$

$$\mathbf{J}_{\omega_i}^{\alpha_t} = \mathbf{J}_{\theta_t}^{\alpha_t} \mathbf{J}_{\omega_i}^{\theta_t} + \mathbf{J}_{\dot{\theta}_t}^{\alpha_t} \mathbf{J}_{\omega_i}^{\dot{\theta}_t} + \mathbf{J}_{\ddot{\theta}_t}^{\alpha_t} \mathbf{J}_{\omega_i}^{\ddot{\theta}_t}, \quad (125)$$

$$\mathbf{J}_{\alpha_i}^{\alpha_t} = \mathbf{J}_{\theta_t}^{\alpha_t} \mathbf{J}_{\alpha_i}^{\theta_t} + \mathbf{J}_{\dot{\theta}_t}^{\alpha_t} \mathbf{J}_{\alpha_i}^{\dot{\theta}_t} + \mathbf{J}_{\ddot{\theta}_t}^{\alpha_t} \mathbf{J}_{\alpha_i}^{\ddot{\theta}_t}, \quad i \in \{a, b\}. \quad (126)$$

REFERENCES

- [1] M. Bosse and R. Zlot, "Continuous 3d scan-matching with a spinning 2d laser," in *2009 IEEE International Conference on Robotics and Automation*. IEEE, 2009, pp. 4312–4319.
- [2] M. Bosse, R. Zlot, and P. Flick, "Zebedee: Design of a spring-mounted 3-d range sensor with application to mobile mapping," *IEEE Transactions on Robotics*, vol. 28, no. 5, pp. 1104–1119, 2012.
- [3] P. Dellenbach, J.-E. Deschaud, B. Jacquet, and F. Goulette, "Ct-icp: Real-time elastic lidar odometry with loop closure," in *2022 International Conference on Robotics and Automation (ICRA)*. IEEE, 2022, pp. 5580–5586.
- [4] T.-M. Nguyen, S. Yuan, M. Cao, Y. Lyu, T. H. Nguyen, and L. Xie, "Ntu viral: A visual-inertial-ranging-lidar dataset, from an aerial vehicle viewpoint," *The International Journal of Robotics Research*, vol. 41, no. 3, pp. 270–280, 2022.
- [5] T.-M. Nguyen, D. Duberg, P. Jensfelt, S. Yuan, and L. Xie, "Slic: Multi-input multi-scale surfel-based lidar-inertial continuous-time odometry and mapping," *IEEE Robotics and Automation Letters*, vol. 8, no. 4, pp. 2102–2109, 2023.
- [6] P. Furgale, T. D. Barfoot, and G. Sibley, "Continuous-time batch estimation using temporal basis functions," in *2012 IEEE International Conference on Robotics and Automation*. IEEE, 2012, pp. 2088–2095.
- [7] P. Furgale, J. Rehder, and R. Siegwart, "Unified temporal and spatial calibration for multi-sensor systems," in *2013 IEEE/RSJ International Conference on Intelligent Robots and Systems*. IEEE, 2013, pp. 1280–1286.
- [8] J. Rehder, J. Nikolic, T. Schneider, T. Hinzmann, and R. Siegwart, "Extending kalibr: Calibrating the extrinsics of multiple imus and of individual axes," in *2016 IEEE International Conference on Robotics and Automation (ICRA)*. IEEE, 2016, pp. 4304–4311.
- [9] L. Oth, P. Furgale, L. Kneip, and R. Siegwart, "Rolling shutter camera calibration," in *Proceedings of the IEEE Conference on Computer Vision and Pattern Recognition*, 2013, pp. 1360–1367.
- [10] A. Patron-Perez, S. Lovegrove, and G. Sibley, "A spline-based trajectory representation for sensor fusion and rolling shutter cameras," *International Journal of Computer Vision*, vol. 113, no. 3, pp. 208–219, 2015.
- [11] E. Mueggler, G. Gallego, H. Rebecq, and D. Scaramuzza, "Continuous-time visual-inertial odometry for event cameras," *IEEE Transactions on Robotics*, vol. 34, no. 6, pp. 1425–1440, 2018.
- [12] X. Lang, J. Lv, J. Huang, Y. Ma, Y. Liu, and X. Zuo, "Ctrl-vio: Continuous-time visual-inertial odometry for rolling shutter cameras," *IEEE Robotics and Automation Letters*, vol. 7, no. 4, pp. 11 537–11 544, 2022.

- [13] K. Li, Z. Cao, and U. D. Hanebeck, "Continuous-time ultra-wideband-inertial fusion," *IEEE Robotics and Automation Letters*, vol. 8, no. 7, pp. 4338–4345, 2023.
- [14] J. Quenzel and S. Behnke, "Real-time multi-adaptive-resolution-surfel 6d lidar odometry using continuous-time trajectory optimization," in *2021 IEEE/RSJ International Conference on Intelligent Robots and Systems (IROS)*. IEEE, 2021, pp. 5499–5506.
- [15] J. Lv, K. Hu, J. Xu, Y. Liu, X. Ma, and X. Zuo, "Clins: Continuous-time trajectory estimation for lidar-inertial system," in *2021 IEEE/RSJ International Conference on Intelligent Robots and Systems (IROS)*. IEEE, 2021, pp. 6657–6663.
- [16] T.-M. Nguyen, X. Xu, T. Jin, Y. Yang, J. Li, S. Yuan, and L. Xie, "Eigen is all you need: Efficient lidar-inertial continuous-time odometry with internal association," *IEEE Robotics and Automation Letters*, vol. 9, no. 6, pp. 5330 – 5337, 2024.
- [17] C. Park, P. Moghadam, J. L. Williams, S. Kim, S. Sridharan, and C. Fookes, "Elasticity meets continuous-time: Map-centric dense 3d lidar slam," *IEEE Transactions on Robotics*, vol. 38, no. 2, pp. 978–997, 2021.
- [18] X. Zheng and J. Zhu, "Traj-llo: A resilient multi-lidar multi-imu state estimator through sparse gaussian process," *arXiv preprint arXiv:2402.09189*, 2024.
- [19] T. Y. Tang, D. J. Yoon, and T. D. Barfoot, "A white-noise-on-jerk motion prior for continuous-time trajectory estimation on se (3)," *IEEE Robotics and Automation Letters*, vol. 4, no. 2, pp. 594–601, 2019.
- [20] X. Yan, V. Indelman, and B. Boots, "Incremental sparse gp regression for continuous-time trajectory estimation and mapping," *Robotics and Autonomous Systems*, vol. 87, pp. 120–132, 2017.
- [21] Y. Wu, D. J. Yoon, K. Burnett, S. Kammel, Y. Chen, H. Vhavle, and T. D. Barfoot, "Picking up speed: Continuous-time lidar-only odometry using doppler velocity measurements," *IEEE Robotics and Automation Letters*, vol. 8, no. 1, pp. 264–271, 2022.
- [22] K. Burnett, A. P. Schoellig, and T. D. Barfoot, "Continuous-time radar-inertial and lidar-inertial odometry using a gaussian process motion prior," *arXiv preprint arXiv:2402.06174*, 2024.
- [23] —, "Imu as an input vs. a measurement of the state in inertial-aided state estimation," *arXiv preprint arXiv:2403.05968*, 2024.
- [24] J. Peršić, L. Petrović, I. Marković, and I. Petrović, "Spatiotemporal multisensor calibration via gaussian processes moving target tracking," *Ieee transactions on robotics*, vol. 37, no. 5, pp. 1401–1415, 2021.
- [25] S. Agarwal and K. Mierle, "Ceres solver: Tutorial & reference." [Online]. Available: <http://ceres-solver.org/>
- [26] T. D. Barfoot, C. H. Tong, and S. Särkkä, "Batch continuous-time trajectory estimation as exactly sparse gaussian process regression," in *Robotics: Science and Systems*, vol. 10. Citeseer, 2014, pp. 1–10.
- [27] T. Qin, P. Li, and S. Shen, "Vins-mono: A robust and versatile monocular visual-inertial state estimator," *IEEE Transactions on Robotics*, vol. 34, no. 4, pp. 1004–1020, 2018.
- [28] C. Forster, L. Carlone, F. Dellaert, and D. Scaramuzza, "On-manifold preintegration for real-time visual-inertial odometry," *IEEE Transactions on Robotics*, vol. 33, no. 1, pp. 1–21, 2016.
- [29] N. Demmel, D. Schubert, C. Sommer, D. Cremers, and V. Usenko, "Square root marginalization for sliding-window bundle adjustment," in *Proceedings of the IEEE/CVF International Conference on Computer Vision*, 2021, pp. 13 260–13 268.
- [30] C. Sommer, V. Usenko, D. Schubert, N. Demmel, and D. Cremers, "Efficient derivative computation for cumulative b-splines on lie groups," in *Proceedings of the IEEE/CVF Conference on Computer Vision and Pattern Recognition*, 2020, pp. 11 148–11 156.
- [31] D. Schubert, T. Goll, N. Demmel, V. Usenko, J. Stueckler, and D. Cremers, "The TUM VI benchmark for evaluating visual-inertial odometry," in *International Conference on Intelligent Robots and Systems (IROS)*, 2018.
- [32] V. Usenko, N. Demmel, and D. Cremers, "The double sphere camera model," in *2018 International Conference on 3D Vision (3DV)*. IEEE, 2018, pp. 552–560.
- [33] W. Zhao, A. Goudar, X. Qiao, and A. P. Schoellig, "Util: An ultra-wideband time-difference-of-arrival indoor localization dataset," *The International Journal of Robotics Research*, p. 02783649241230640, 2022.
- [34] M. Grupp, "evo: Python package for the evaluation of odometry and slam." <https://github.com/MichaelGrupp/evo>, 2017.
- [35] T.-M. Nguyen, S. Yuan, T. H. Nguyen, P. Yin, H. Cao, L. Xie, M. Wozniak, P. Jensfelt, M. Thiel, J. Ziegenbein, and N. Blunder, "Mcd: Diverse large-scale multi-campus dataset for robot perception," in *Proceedings of the IEEE/CVF Conference on Computer Vision and Pattern Recognition*, Jun. 2024. [Online]. Available: <https://mcdviral.github.io/>
- [36] W. Yu, J. Xu, C. Zhao, L. Zhao, T.-M. Nguyen, S. Yuan, M. Bai, and L. Xie, "I2ekf-lo: A dual-iteration extended kalman filter based lidar odometry," in *2024 IEEE/RSJ International Conference on Intelligent Robots and Systems (IROS)*. IEEE, 2024.
- [37] X. Zheng and J. Zhu, "Traj-llo: In defense of lidar-only odometry using an effective continuous-time trajectory," *IEEE Robotics and Automation Letters*, 2024.
- [38] X. Liu, C. Yuan, and F. Zhang, "Targetless extrinsic calibration of multiple small fov lidars and cameras using adaptive voxelization," *IEEE Transactions on Instrumentation and Measurement*, vol. 71, pp. 1–12, 2022.
- [39] J. Li, T.-M. Nguyen, S. Yuan, and L. Xie, "Pss-ba: Lidar bundle adjustment with progressive spatial smoothing," *arXiv preprint arXiv:2403.06124*, 2024.
- [40] K. Li, M. Li, and U. D. Hanebeck, "Towards high-performance solid-state-lidar-inertial odometry and mapping," *IEEE Robotics and Automation Letters*, vol. 6, no. 3, pp. 5167–5174, 2021.
- [41] Y. Cai, W. Xu, and F. Zhang, "ikd-tree: An incremental kd tree for robotic applications," *arXiv preprint arXiv:2102.10808*, 2021.
- [42] C. Yuan, W. Xu, X. Liu, X. Hong, and F. Zhang, "Efficient and probabilistic adaptive voxel mapping for accurate online lidar odometry," *IEEE Robotics and Automation Letters*, vol. 7, no. 3, pp. 8518–8525, 2022.
- [43] D. Duberg and P. Jensfelt, "UFOMap: An efficient probabilistic 3D mapping framework that embraces the unknown," *IEEE Robotics and Automation Letters*, vol. 5, no. 4, pp. 6411–6418, 2020.
- [44] J. Jiao, H. Ye, Y. Zhu, and M. Liu, "Robust odometry and mapping for multi-lidar systems with online extrinsic calibration," *IEEE Transactions on Robotics*, vol. 38, no. 1, pp. 351–371, 2021.
- [45] J. Sola, J. Deray, and D. Atchuthan, "A micro lie theory for state estimation in robotics," *arXiv preprint arXiv:1812.01537*, 2018.